Coherent Multistatic UAV-Based SAR

Julian Kanz, *Graduate Student Member, IEEE*, Christina Bonfert, *Member, IEEE*, Christian Gesell, *Graduate Student Member, IEEE*, Alexander Grathwohl, *Graduate Student Member, IEEE*, Frederik Bormuth, *Graduate Student Member, IEEE*, Gerhard Krieger, *Fellow, IEEE*, and Christian Waldschmidt, *Fellow, IEEE*

***Abstract*—Multistatic synthetic aperture radar (SAR) with uncrewed aerial vehicles (UAVs) as platforms enables applications not possible with monostatic SAR by spatially separating transmitter and receiver. Single-pass interferometry and tomography or the analysis of different scattering mechanisms becomes feasible while having the large flexibility of UAV-based systems. To fully exploit the advantages, the single nodes have to operate cooperatively. Coherency is required in time, frequency, and phase. In conventional approaches, these requirements necessitate high synchronization accuracies. In this work, a highly scalable concept is introduced that uses receive (Rx)-only nodes and a dedicated transmitter in contrast to typical passive radar techniques. Radar and reference signal required for demodulation are received, directly sampled, and stored locally onboard the UAV. The high demands on timing accuracy translate into localization accuracy, which is needed for SAR processing anyway. Coherency is created in postprocessing by digital demodulation, allowing for phase coherent SAR imaging. The processing steps are explained, and the influence of possible error sources is analyzed. The concept is validated by static radar measurements and a bistatic UAV-based SAR experiment of a realistic scenario.**

***Index Terms*—Bistatic, chirp-sequence modulation, coherency, frequency-modulated continuous-wave (FMCW) radar, multistatic, passive radar, radar systems, signal processing, synthetic aperture radar (SAR), uncrewed aerial vehicle (UAV).**

I. Introduction

THE integration of radar technology onto uncrewed aerial vehicles (UAVs) represents a significant advancement in remote sensing, enabling operations in environments hardly accessible. In addition, short revisit times are possible, enabling the recording of time series.

Various applications of UAV-based radar imaging have evolved in the past years [1]. These systems are used for climate research [2], snow depth estimation [3], ice-penetrating radar [4], and detection of avalanche victims or people in collapsed buildings [5], [6].

Synthetic aperture radar (SAR) enhances radar imaging by exploiting the movement of the UAV to improve the resolution. This has been proven to be feasible for landmine detection [7], quantification of surface displacements [8], interferometry [9], detection of foreign objects on airport runways [10], and a variety of other applications [2], [11], [12], [13], [14], [15].

Complementary information can be obtained by deploying bistatic SAR, where transmit and receive nodes are spatially separated. This allows for applications such as single-pass interferometry [16] or tomography [17], wind speed estimation [18], soil moisture retrieval [19], [20], analysis of glacial snow covers [21], or the estimation of 3-D displacement vectors [22].

Bistatic SAR on UAVs has been demonstrated recently for tomography [23], 3-D localization of objects [24], and measurement of snow volumes [25]. Moreover, multistatic SAR offers the opportunity to use a swarm of UAVs for cooperative sensing.

However, multistatic SAR imaging requires the synchronization of distributed nodes to coherently process radar signals. Conventional methods in multistatic radar use hardware synchronization by either distributing high-frequency radar signals [26], [27] or sharing reference signals between the nodes [28], [29], [30], [31]. The symmetry of occurring errors can be exploited by both Tx and Rx with each node [32], [33], [34] or by operating the sensors uncoupled while establishing coherency in postprocessing [28], [31], [35], [36], [37], [38]. However, to achieve synchronization precise enough in a moving scenario like a swarm of UAVs, only atomic onboard reference clocks or fiber optic cables between UAVs are currently feasible [39]. GNSS-derived oscillators have also been proven feasible for bistatic SAR imaging on UAVs [25]; however, they require valid GNSS data throughout the measurement.

There are also approaches, which do not require any synchronization, such as repeater-based concepts [24], [40], [41], [42], or passive radars [43], [44], [45], [46], [47], [48], [49], [50]. Passive radar concepts suffer from inflexibility due to the fixed frequency range and bandwidth of the illuminators of opportunity used as transmitter. This issue can be circumvented by providing a dedicated transmitter with carefully chosen signal parameters suited for radar imaging.

Synchronization of the single nodes within a multistatic radar network is also commonly done using a reference link between the nodes. This approach has been realized in satellite systems like TanDEM-X [16], [51] as well as in ground-based systems [29]. The direct link can be used as a reference path too, where a copy of the radar signal is transmitted. With the use of this second reference path, absolute range information can be obtained [52]. However, in [52], the reference signal is

Received 20 February 2025; revised 10 April 2025 and 7 June 2025; accepted 25 July 2025. Date of publication 30 July 2025; date of current version 11 August 2025. This work was supported by the Deutsche Forschungsgemeinschaft (DFG, German Research Foundation) through the Project GRK 2680 under Grant 437847244. *(Corresponding author: Julian Kanz.)*

Julian Kanz, Christina Bonfert, Christian Gesell, Alexander Grathwohl, Frederik Bormuth, and Christian Waldschmidt are with the Institute of Microwave Engineering, Ulm University, 89081 Ulm, Germany (e-mail: julian.kanz@uni-ulm.de).

Gerhard Krieger is with the Microwaves and Radar Institute, German Aerospace Center (DLR), 82234 Weßling, Germany.

Digital Object Identifier 10.1109/TRS.2025.3593818

used to estimate the time of flight (ToF), but not to coherently demodulate the Rx signal. A similar concept is shown by Ash et al. [53], where the radar signal is also transmitted via two paths and then demodulated by mixing both the signals. This approach is referred to as over-the-air deramping (OTAD). Lee et al. [54] developed hardware to deploy this concept onboard UAVs. However, only the deramped low-frequency signal is recorded, which offers few possibilities for error correction, since demodulation already occurred.

This article introduces a concept, in which the signal is transmitted via two paths, the desired radar path and the direct line-of-sight (LoS) path. The high-frequency (RF) Rx signal is directly sampled, stored locally, and coherent demodulation is performed in postprocessing. Both the signals are combined in the analog domain and sampled, preventing unnecessary data to be stored. Demodulation is performed in the digital domain by squaring the combined signal.

Thereby, the required synchronization accuracy is reduced significantly compared with conventional approaches. This is because only radar and localization data need to be allocated for SAR processing. In contrast to wireless synchronization or repeater-based approaches, no multiplexing is required, resulting in an easily scalable concept.

Starting from Rx-only nodes, this article introduces the concept of using a digital receiver for multistatic SAR imaging. The radar signal is transmitted via two paths and directly sampled at the receiver node. A signal model is defined and the steps of digital demodulation are described. Possible error sources are explained and methods to reduce their impact are pointed out. It is shown that the proposed concept is suited for SAR processing. The influence of relevant errors and methods to compensate them are demonstrated.

After describing the system concept in Section II, the coherent demodulation is explained in Section III. The single sensor radar concept is expanded in Section IV to enable multistatic SAR imaging. The concept is validated with static radar measurements and UAV-borne SAR measurements in Section V.

II. System Concept

This section aims to introduce the system concept of Rx-only nodes for multistatic SAR imaging in large swarms of UAVs. The process of establishing coherency in frequency, time, and phase is explained, and requirements on localization and synchronization as well as on the system configuration are discussed. Finally, constraints on the geometry are introduced, to further investigate and compare the performance of various flight formations.

A. Rx-Only Nodes for Coherent Multistatic SAR

Multistatic concepts based on wireless synchronization or joint processing on one node combined with repeater nodes are hard to scale for large swarms of UAVs. This is due to the multiplexing necessary to prevent interference of signals from different nodes. Fig. 1 illustrates the Rx-only concept introduced in this work for two UAVs with one transmit and one receive node.

The transmit signal is distributed not only on the desired sensing path but also via the direct path between the nodes.

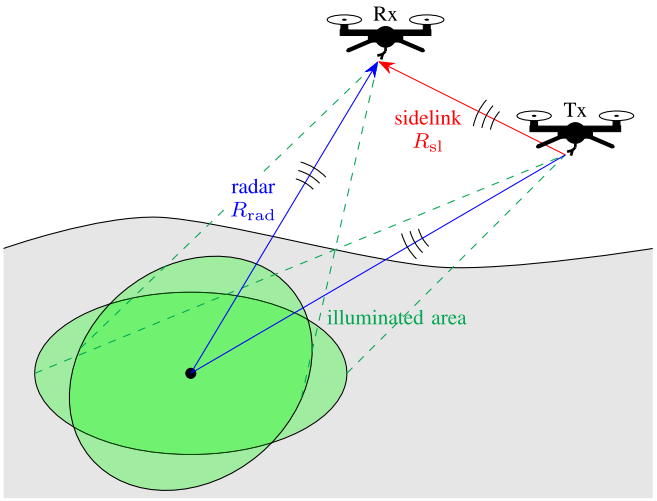

Fig. 1. Illustration of the receive-only concept for one transmit (Tx) and one receive (Rx) node with the path lengths R_{rad} and R_{sl} for the radar and sidelink path, respectively.

This direct reference path is referred to as sidelink in the following.

Receive-only nodes receive both the radar and sidelink signal simultaneously, while their ToF differs due to different geometric path lengths R_{rad} and R_{sl} of the two-way radar and one-way sidelink signal, respectively. Since the sidelink path is the direct link between two nodes, the following condition is always fulfilled:

$$R_{\mathrm{rad}} \geq R_{\mathrm{sl}}. \tag{1}$$

The sidelink signal is used as a reference for demodulation of the radar signal.

Monostatic radar processing uses the known transmit signal to demodulate the received radar signal. In the proposed multistatic setup, the transmit signal is available at the receiver nodes too, only shifted in time by the ToF of the sidelink path. For that reason, the concept is independent of a particular modulation.

In contrast to approaches with two synchronized radar nodes, the range relative to the sidelink path length

$$R_{\mathrm{meas}} = R_{\mathrm{rad}} - R_{\mathrm{sl}} \tag{2}$$

is measured in this concept. This is because the sidelink signal serves as the reference signal for demodulation. The negative range offset is later corrected for relying on precise localization data of the single nodes, which is required for SAR processing anyway. The estimated radar path length $\hat{R}_{\mathrm{rad}}$ is then obtained by adding the estimated sidelink distance $\hat{R}_{\mathrm{sl}}$

$$\hat{R}_{\mathrm{rad}} = R_{\mathrm{meas}} + \hat{R}_{\mathrm{sl}} = R_{\mathrm{rad}} - R_{\mathrm{sl}} + \hat{R}_{\mathrm{sl}}. \tag{3}$$

In contrast to conventional passive radar concepts, where illuminators of opportunity like GNSS or DVB-T are used as transmit signals, the transmit signal is specifically designed for the sensing purpose in this concept. Problems like a predefined frequency range, restricted bandwidth, or limitations in the acquisition geometry due to fixed transmit nodes can thus be avoided.

Demodulation of the radar receive signal is performed digitally. At the receiver, both the radar signal and the reference

signal are received simultaneously and converted into the digital domain by sampling at an ADC.

The RF signal is available as digitalized sample values, allowing for preprocessing steps before demodulation. Since both the receive signals rely on the same transmit signal, deviations like a frequency offset or phase noise are the same for all received signals.

Knowledge of the parameters of the radar signal is not required at the receiver nodes. If the hardware is suitable for the desired frequency range, the start frequency, bandwidth, and chirp rate can be changed without changing the receiver hardware. Scaling to a large swarm of UAVs is done using more than one UAV-based receive-only node. Due to the passive receive concept, no multiplexing is required, only the sidelink signal must be available at each receive node. This can be achieved, for example, via several dedicated antennas or one omnidirectional antenna. When designing the formation, it must be ensured that the sidelink is not obstructed and the antenna pattern is appropriate.

B. Coherency

Radar imaging with distributed nodes requires coherency in time, frequency, and phase [55]. All three types of coherency are jointly resolved by receiving the radar signal via two ways, in which the ToF of one is known precisely. Timing conditions are translated into localization requirements and frequency and phase coherency is ensured by demodulating with the time-shifted transmit signal.

The impact of phase noise and linearity of the radar signal is the same as for monostatic radars. For range correlation effects of the phase noise, the requirements may even be relaxed in the multistatic setup by choosing the geometry appropriately. According to (2) only a relative range R_{meas} is measured, which is smaller than the radar range R_{rad}. For long-range radar scenarios in particular, this effect may be significant and phase noise can be reduced.

C. Timing Requirements

As shown in (3), the accuracy of the radar measurement relies on a precise sidelink distance estimation. In contrast, time-based synchronization approaches rely on a minimal timing offset between the nodes.

The required localization accuracy for monostatic UAV-based SAR depends on bandwidth and center frequency of the radar signal [56]. A maximum tolerable one-way range offset of $\delta R_{\max} = 2$ cm is assumed to derive the maximum timing offset. For a center frequency of 1.4 GHz, as used in the subsequent experiments, this corresponds to approximately $\lambda/10$. The derivation and justification of this value are provided in Section IV-D, where it is shown that for errors above this value SAR images become degraded and targets are no longer focused. The range offset affects both the transmit and receive path. This results in a maximum range error of $2\delta R_{\max}$ in the worst case.

To achieve the same accuracy with time-based synchronization, the allowed timing offset between the nodes is given by

$$\delta t_{\max,\text{sync}} = 2\delta R_{\max}/c_0 \approx 133 \text{ ps}. \tag{4}$$

If the time reference is only used to allocate measurements of different receive nodes for joint processing, the timing error should not exceed the pulse repetition interval T_{pri}. The allowed timing offset is

$$\delta t_{\max,\text{pri}} = T_{\text{pri}} = 1/f_{\text{prf}} = 10 \text{ ms} \tag{5}$$

for an exemplary pulse repetition frequency $f_{\text{prf}} = 100$ Hz as deployed in our system. However, the more stringent boundary for $\delta t_{\max}$ is now determined by the localization error introduced when localization data are time-stamped with erroneous time data. The movement of the UAV translates timing errors to localization errors. The resulting limit can be approximated by

$$\delta t_{\max,\text{loc}} = 2\delta R_{\max}/v_{\max} = 4 \text{ ms} \tag{6}$$

where v is the platform velocity and a maximum velocity $v_{\max} = 10\frac{\text{m}}{\text{s}}$ is assumed. A relaxation of the timing accuracy of approximately seven orders of magnitude is achieved.

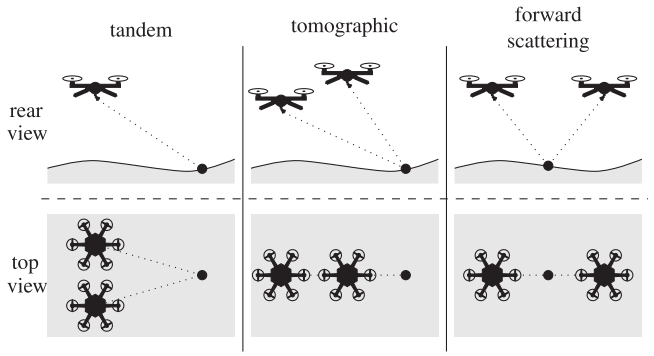

Fig. 2. Geometrical illustration of the investigated UAV formations.

D. Geometric Constraints

The presented concept requires an LoS path between each pair of transmitter and receiver. For a swarm of UAVs conducting a joint acquisition, this is a feasible requirement.

In addition to the properties of the radar sensor and the flight trajectory, the formation geometry provides another degree of freedom, which can be used to enhance SAR imaging. Single-pass interferometry and tomography as well as a forward scattering geometry allow for obtaining height information [17], [24]. Furthermore, complementary information may be gained through different bistatic angles.

To compare the performance of the concept for different realistic scenarios, three defined flight formations are introduced. These are illustrated in Fig. 2 showing rear and top view each. Here, the rear view indicates a plane orthogonal to the flight direction. Note that bistatic geometries with one transmitter and one receiver are considered. Multistatic geometries are obtained by combining bistatic pairs.

The tomographic formation is suitable for single-pass tomography or interferometry, the tandem formation for imaging with varying bistatic angles, and the forward scattering geometry for resolving the third dimension or analyzing scattering mechanisms. These formations are analyzed and compared in Section IV.

III. Digital Demodulation

In this section, a frequency-modulated continuous-wave (FMCW) modulation is assumed. First, a model of the received

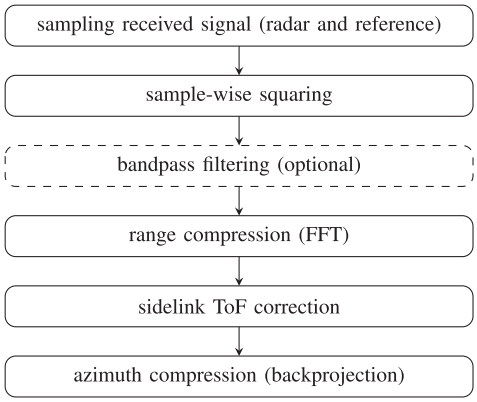

Fig. 3. Flowchart of the signal processing chain for SAR imaging with the digital Rx-only concept.

signal for an arbitrary number of targets is introduced. The steps of digital demodulation are explained subsequently.

Fig. 3 shows the signal processing chain required to evaluate the sampled signals. The first four steps representing the processing of single radar measurements are described in detail in this section. The last step combines the single measurements coherently to form a synthetic aperture, which is explained in detail in Section IV.

A. Signal Model

The transmit signal of the mth radar measurement is an FMCW chirp and is described by

$$s_{\mathrm{Tx}}(t) = a_{\mathrm{Tx}} \cos\left(\phi_{\mathrm{Tx}}(t)\right), \quad 0 \le t - mT_{\mathrm{pri}} \le T \tag{7}$$

where a_{Tx} represents the amplitude, T the chirp duration, T_{pri} the pulse repetition interval, and

$$\phi_{\mathrm{Tx}}(t) = 2\pi f_0 t + \pi K_r t^2 + \phi_0 \tag{8}$$

the instantaneous phase of the chirp with start frequency f_0, chirp rate K_r, and start phase ϕ_0. The frequency is obtained by the derivation of the phase over time

$$f_{\mathrm{Tx}}(t) = \frac{1}{2\pi}\frac{\partial \phi_{\mathrm{Tx}}}{\partial t} = f_0 + K_r t. \tag{9}$$

The signal is split and transmitted simultaneously via both the radar and the sidelink path. A scene with an arbitrary number of N targets or scattering centers is assumed. The received signal is a superposition of the direct sidelink signal and the returns from each of the targets. It is described by

$$\begin{aligned} s_{\mathrm{Rx}}(t) &= s_{\mathrm{Rx,sl}}(t) + \sum_{n=1}^{N} s_{\mathrm{Rx},n}(t) \\ &= a_{\mathrm{sl}} \cos\left(\phi_{\mathrm{Rx,sl}}(t)\right) + \sum_{n=1}^{N} a_n \cos\left(\phi_{\mathrm{Rx},n}(t)\right) \end{aligned} \tag{10}$$

where the index sl refers to the sidelink component and n to the backscattered signal from the nth target. The frequency of the sidelink signal components is given by

$$f_{\mathrm{Rx,sl}}(t) = f_{\mathrm{Tx}}(t - \Delta t_{\mathrm{sl}}) \tag{11}$$

where

$$\Delta t_{\mathrm{sl}} = \frac{R_{\mathrm{sl}}}{c_0} \tag{12}$$

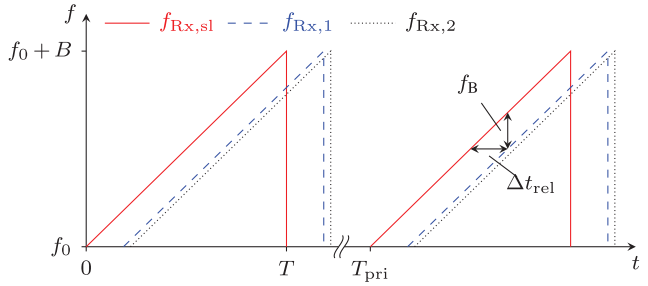

Fig. 4. Schematic representation of the received FMCW signal with start frequency f_0, bandwidth B, chirp duration T, and pulse repetition interval T_{pri} for an exemplary two-target scenario.

is the ToF of the sidelink signal. Similarly, the frequency of the target signal components is

$$f_{\mathrm{Rx},n}(t) = f_{\mathrm{Tx}}(t - \Delta t_n) \tag{13}$$

where

$$\Delta t_n = \frac{R_{\mathrm{Tx},n} + R_{\mathrm{Rx},n}}{c_0}, \quad n = 1, \ldots, N \tag{14}$$

are the ToFs of the target signals. The relative velocities of the targets to the sensor platform are neglected, as its impact is orders of magnitude smaller than the range-dependent terms. Note that the ToF of the sidelink signal is always smaller than the ToF of the scattered signals.

The difference in ToF can be derived by subtracting (14) and (12)

$$\Delta t_{\mathrm{rel},n} = \Delta t_n - \Delta t_{\mathrm{sl}} = \frac{R_{\mathrm{Tx},n} + R_{\mathrm{Rx},n} - R_{\mathrm{sl}}}{c_0}. \tag{15}$$

This relative ToF is measured by the radar and its value can be controlled by the acquisition geometry.

In Fig. 4, the frequencies of the received signal components introduced in (11) and (13) are depicted over time. An exemplary two-target scenario is assumed, where targets 1 and 2 act as boundaries for the targets with minimum and maximum ranges. The exemplary relative ToF Δt_{rel} illustrated causes signal components with beat frequency f_B when demodulating the received signal. This is derived in Section IV-B

The sampling values of the received signal in (10) are stored locally and form the input of the subsequent digital processing. By controlling the data recording, e.g., triggered by detecting a chirp [57] or a known transmitted sequence, storing samples without valid measurement data can be prevented.

B. Squaring of Received Signal

To obtain the desired modulation products, the sidelink signal is multiplied with the single radar signals

$$s_{\mathrm{dem,des}}(t) = s_{\mathrm{Rx,sl}}(t) \cdot \sum_{n=1}^{N} s_{\mathrm{Rx},n}(t). \tag{16}$$

In practice, this approach is prone to errors, because the sidelink signal couples in the radar antenna and vice versa. Furthermore, two separate channels would be needed to separately store sidelink and radar signal, resulting in twice the amount of data.

For this reason, sidelink and radar signal are combined in the analog domain and only one Rx channel is deployed. The

superimposed signal is sampled at the ADC and stored locally. Another reason is that potential sample frequency offsets are prevented, which can occur if two different channels are used.

The combined signal is then squared samplewise to demodulate the signal

$$s_{\mathrm{dem}}(t) = s_{\mathrm{Rx}}(t)^2 . \tag{17}$$

The principle of squaring a superimposed signal for demodulation is known from single-ended diode mixers [58]. In contrast to the analog squaring due to nonlinearities, demodulation here is performed in the digital domain. This allows preprocessing of the stored RF signal before demodulation.

Combining (10) and (17), the demodulated received signal can be derived. Applying the generalized multinomial formula, this results in

$$\begin{aligned} s_{\mathrm{dem}}(t) = s_{\mathrm{Rx}}(t)^2 = \overbrace{s_{\mathrm{Rx,sl}}(t)^2}^{\mathrm{I}} + \overbrace{2\sum_{n=1}^{N} s_{\mathrm{Rx,sl}}(t)\, s_{\mathrm{Rx},n}(t)}^{\mathrm{II}} \\ + \underbrace{\sum_{n=1}^{N} s_{\mathrm{Rx},n}(t)^2}_{\mathrm{III}} + \underbrace{2\sum_{k=1}^{N-1}\sum_{l=k+1}^{N} s_{\mathrm{Rx},k}(t)\, s_{\mathrm{Rx},l}(t)}_{\mathrm{IV}} . \end{aligned} \tag{18}$$

The different signal components are investigated in detail in the following. The squared signals (I and III) are similar and differ only by the subscript. For signal I, this can be expressed as

$$\begin{aligned} \mathrm{I\ (III)}: s_{\mathrm{Rx,sl}}(t)^2 &= a_{\mathrm{sl}}^2 \cos\left(\phi_{\mathrm{Rx,sl}}(t)\right)^2 \\ &= \frac{a_{\mathrm{sl}}^2}{2}\left[\underbrace{1}_{\mathrm{DC}} + \underbrace{\cos\left(2\phi_{\mathrm{Rx,sl}}(t)\right)}_{\mathrm{chirp}}\right]. \end{aligned} \tag{19}$$

Two signal components can be observed, a dc component and a chirp with twice the chirp rate of the transmit signal. Its frequency is expressed by

$$f_{\mathrm{Rx,sl,2}} = \frac{1}{2\pi}\cdot 2 \cdot \frac{\partial \phi_{\mathrm{Rx,sl}}}{\partial t} = 2f_0 + 2K_r\left(t - \Delta t_{\mathrm{sl}}\right). \tag{20}$$

Both dc signal and chirp can be filtered digitally and are not considered in the following processing steps. The same holds for the squared radar signals $s_{\mathrm{Rx},n}$.

The modulation signals (II and IV) differ only by the subscript similar to parts I and III above. For signal II, this results in

$$\begin{aligned} \mathrm{II\ (IV)}: s_{\mathrm{Rx,sl}}(t)\, s_{\mathrm{Rx},n}(t) = \frac{a_{\mathrm{sl}} a_n}{2}\Bigg[\overbrace{\cos\left(\phi_{\mathrm{Rx,sl}}(t) + \phi_{\mathrm{Rx},n}(t)\right)}^{\mathrm{chirp}} \\ + \underbrace{\cos\left(\phi_{\mathrm{Rx,sl}}(t) - \phi_{\mathrm{Rx},n}(t)\right)}_{\mathrm{beat\ signal}}\Bigg]. \end{aligned} \tag{21}$$

Again, the first component represents a chirp with twice the start frequency and chirp rate. The second part of the signal is the demodulated chirp, i.e., the desired beat signal.

A generalized expression of the beat signal is given by

$$s_B(t) = \frac{a_k a_l}{2}\cos\left(\phi_B(t)\right) \tag{22}$$

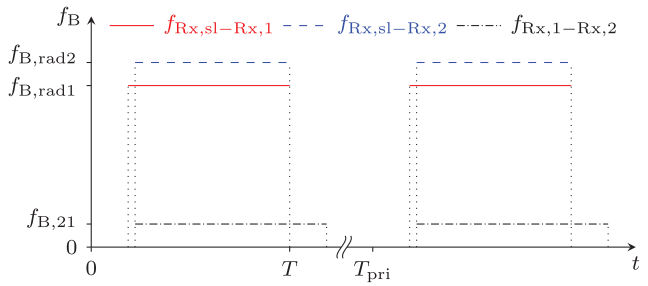

Fig. 5. Schematic representation of the beat frequency components of the squared Rx signal for the exemplary two-target scenario introduced in Fig. 4.

with

$$\begin{aligned} \phi_B(t) &= \phi_{\mathrm{Rx},k}(t) - \phi_{\mathrm{Rx},l}(t) \\ &= -2\pi\left(f_0 + K_r t\right)\left(\Delta t_k - \Delta t_l\right) + \pi K_r\left(\Delta t_k^2 - \Delta t_l^2\right) \\ &\approx -2\pi\left(f_0 + K_r t\right)\left(\Delta t_k - \Delta t_l\right) \end{aligned} \tag{23}$$

where the indices k and l can correspond to either two radar signals or one radar and the sidelink signal. The simplification made above is valid for $\Delta t_k \ll t$.

The beat frequency is described by

$$f_B = \frac{1}{2\pi}\frac{\partial \phi_B(t)}{\partial t} = -K_r\left(\Delta t_k - \Delta t_l\right) = -\frac{K_r}{c_0}\left(R_k - R_l\right) \tag{24}$$

where R_k is the total range of the path corresponding to the index k. Each beat frequency in the demodulated signal is thus proportional to a range difference. This can be either a difference in sidelink range and radar range or two radar ranges. Note that R_k denotes a two-way range for radar signals and a one-way range for the sidelink signal.

Fig. 5 illustrates the beat frequency components of the demodulated signal based on the two-target scenario assumed in Fig. 4.

C. Intermodulation Products

In addition to the desired modulation products, the demodulated signal contains undesired products that may affect the performance. An exemplary demodulated signal is illustrated in Fig. 5, where the undesired product corresponds to the component with the frequency $f_{B,21}$. In the following, the undesired products are referred to as intermodulation products in contrast to modulation products that are desired.

From (24), it can be concluded that all occurring beat frequencies are proportional to a difference in ranges. Modulation products are represented by the difference in a radar range $R_{\mathrm{rad},k}$ and the sidelink range R_{sl}, intermodulation products by the difference in two radar ranges $R_{\mathrm{rad},k}$ and $R_{\mathrm{rad},l}$.

Intermodulation products can result in ghost targets at a range that equals the difference in two radar ranges. Only if all differences in radar ranges are outside the evaluated range spectrum, unambiguous imaging is possible. By appropriately choosing the acquisition geometry, the unambiguous range section can be controlled. The influence of intermodulation products on SAR imaging is explained in detail in Section IV-C.

Intermodulation products outside the evaluated part of the range spectrum are removed by bandpass filtering. This step is, however, optional, as intermodulation products at ranges

not evaluated in the subsequent processing do not influence the imaging.

D. Range Compression

After demodulation by squaring, range compression is performed to transfer the superimposed beat signal into range information. This is done by applying a fast Fourier transform (FFT) along the fast time samples for each chirp.

The processing follows the steps explained in [41]. The resulting range-compressed signal of the mth measurement for a single-target case is given by

$$S_{B,m}(R) = T\,\mathrm{sinc}\left[T\left(\frac{2K_r(R-R_m)}{c_0}\right)\right] \cdot \exp\left[j\phi_B(R,R_m)\right] \tag{25}$$

with

$$\phi_B(R,R_m) = \frac{4\pi f_0 R_m}{c_0} - \frac{2\pi K_r T(R-R_m)}{c_0} - \frac{4\pi K_r R_m}{c_0^2}(2R-R_m) \tag{26}$$

where R_m is the target range relative to the sidelink range and R is the range axis of the range-compressed signal. R_m corresponds to the one-way measured range $R_{\mathrm{meas}}/2$ from (2), which varies for every single measurement m. The factor 2 ensures one-way ranges to be considered and thus comparability to standard monostatic radar processing algorithms.

For the conversion of the beat frequency f_B into range information, the knowledge of the chirp rate K_r is required. This is the only parameter of the FMCW radar signal that has to be known in the signal processing.

E. Range Offset Correction

From (2), it can be stated that only a range relative to the sidelink is measured. This has to be corrected to use the accurate geometric information for subsequent SAR processing; see (3).

In practice, R_{sl} is not a constant offset during the measurement, even when flying in a constant formation. Because of fluctuations in movement and heading due to wind, the sidelink distance has to be estimated and corrected for every single measurement m. These data are available because localization data are required for each measurement to apply SAR processing.

IV. SAR Processing

Section III showed the coherent demodulation and range compression of single multistatic radar measurements. The phase coherence between the individual measurements is next used for synthetic aperture processing.

In this section, the single steps of the processing are explained to create an unambiguous SAR image from range-compressed radar data and localization data. Subsequently, the influence of intermodulation products, localization errors, and amplitude deviations is investigated.

A. Allocation of Radar and Localization Data

Following the processing steps explained in Section III, range-compressed data with absolute range information are provided. For each single measurement, localization data of all nodes are required as well to generate an SAR image.

For this purpose, both radar and localization data are time-stamped with a common time reference. Here, GNSS time is used for this purpose. The required accuracy is dependent on the platform velocity, as timing errors result in position offsets due to the movement of the UAV.

B. Backprojection

Azimuth compression of the range-compressed data is done via time-domain backprojection [59]. This approach does not make any assumptions about the geometry and is thus well-suited for multistatic UAV-based SAR [2]. The processing follows the extended backprojection algorithm described by Grathwohl et al. [41] without the repeater-specific demodulation step.

The area where the SAR image should be created is divided into pixels, and for each pixel and acquisition, the range-dependent expected phase is calculated. This phase is then subtracted from the measured phase by multiplication of (25) with a complex exponential term and subsequent summation over the single measurements m

$$A(\mathbf{x_0}) = \sum_m S_{B,m}(R_m)\exp\left[-j\phi_e(R_m)\right] \tag{27}$$

where $A(\mathbf{x_0})$ is the complex pixel value at the position $\mathbf{x_0}$ in the SAR image and

$$\phi_e(R_m) = \phi_B(R_m,R_m) = \frac{4\pi f_0 R_m}{c_0} - \frac{4\pi K_r R_m^2}{c_0^2} \tag{28}$$

the expected phase for the range R_m with $\phi_B(R,R_m)$ given in (26). If a scatterer is located at the range R_m, the phase of $S_{B,m}(R_m)$ equals $\phi_e(R_m)$. Given the pixel location $\mathbf{x_0}$ of the scatterer, this holds for all m and a large amplitude in the SAR image is obtained.

Note that for linear SAR, the range progression along the trajectory is described by a hyperbola. Hence, azimuth compression by backprojection corresponds to a phase-coherent integration over such a hyperbola. This shape of the integration path is important when analyzing the intermodulation products, as shown in the following.

C. Suppression of Intermodulation Products

In the range-compressed data, both modulation and intermodulation products occur, as explained in Section III-C. For a number of acquisitions along a trajectory, all these products have distinct range progressions, as range varies along the trajectory.

There are three ways to ensure the suppression of the intermodulation products, resulting in an unambiguous SAR image. These approaches are described in detail in the following.

1) Choosing an Appropriate Geometry: The range at which intermodulation products occur can be controlled by the geometry, i.e., the flight formation of the UAVs. In the backprojection algorithm, only radar returns at those ranges R_m are evaluated, which correspond to the distance between

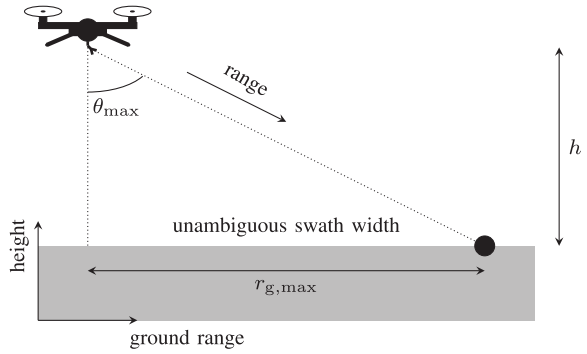

Fig. 6. Monostatic geometry for the derivation of the maximum unambiguous swath width.

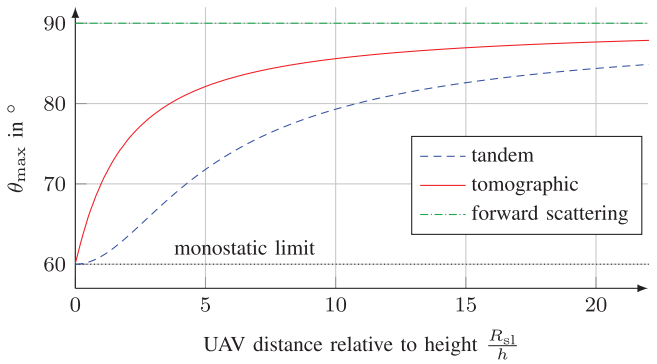

Fig. 7. Maximum elevation angle for which SAR imaging is not affected by any modulation products for a monostatic geometry and the three considered multistatic formations.

radar and pixel. This can be seen in (27). Thus, by choosing a geometry, where no intermodulation products occur at the evaluated ranges R_m, unambiguous SAR images are created.

Assuming a side-looking geometry with a depression angle of 45°, the unambiguous swath width can be derived for a monostatic geometry and the three formations introduced in Section II-D.

First, the unambiguous swath width is derived for a monostatic geometry, i.e., transmitter and receiver nodes are located at the same point in space. The geometry used in the derivation is shown in Fig. 6.

The minimum range with expected radar backscatter is given by the height h of the UAV, which corresponds to the nadir return. The maximum range is dependent on the maximum elevation angle $\theta_{\max}$, defining the maximum swath width. Note that the elevation angle is measured relative to the vertical, with 0° representing nadir and 90° a horizontal signal path.

For unambiguous imaging, the following condition has to be fulfilled:

$$R_{\max} - R_{\min} = h\left(\frac{1}{\cos(\theta_{\max})} - 1\right) \overset{!}{\leq} h = R_{\min}. \tag{29}$$

This means that the maximum range difference has to be smaller than the minimum range evaluated in the backprojection algorithm. Thus, all the intermodulaton products occur at ranges that are not evaluated.

For the monostatic geometry, solving (29) results in $\theta_{\max} = 60°$ and a maximum unambiguous swath width

$$r_{g,\max} = h\tan(\theta_{\max}) = \sqrt{3}\cdot h \approx 1.73\cdot h \tag{30}$$

measured from nadir.

For the multistatic formations, i.e., tandem, tomographic, and forward scattering, $\theta_{\max}$ is derived the same way. In every case, one UAV is fixed at the monostatic position indicated in Fig. 6. The other UAV is moved with increasing relative distance. In the tandem case, the center point between both the UAVs is constant, while the UAVs are moved apart in the azimuth direction. The second UAV in the tomographic formation is moved along a line orthogonal to slant range while increasing its height. The azimuth position remains the same. In the forward scattering formation, the center point is fixed and the height of both the UAVs is increased while retaining the depression angle of 45°. In the latter case, only the area in ground range between the UAVs is considered as swath.

For the tandem case, the maximum unambiguous range is derived in the Appendix

$$r_{g,\max} = \frac{1}{2}\sqrt{3R_{sl}^2 + 12h^2}. \tag{31}$$

Note that the monostatic result (30) represents a special case of (31) for $R_{sl} = 0$.

The result is dependent on the relative distance of both the UAVs and is shown in Fig. 7. With increasing relative distance of the UAVs, $\theta_{\max}$ and thus the unambiguous swath width can be increased. In case of forward scattering, the condition for unambiguous imaging is fulfilled for all distances, indicated by a maximum elevation angle $\theta_{\max} = 90°$. The tandem and tomographic formation behave like one monostatic node for small distances and converge to the forward scattering case for large distances. Saturation is reached at smaller angles in the tomographic case. This behavior can be easily explained by the geometry assumed for the derivation.

By moving the UAVs apart and increasing the bistatic angle, i.e., the angle between the radar transmit and receive paths, the unambiguous swath width can be increased. Unambiguous imaging up to a swath width of $(3)^{1/2}\cdot h$ is possible in any case.

2) Influence of the Integration Path: If the unambiguous swath width is not large enough, the coherent integration in SAR processing can be used to suppress intermodulation products. The range progression of modulation products is described by a hyperbola along the azimuth direction y in a monostatic geometry

$$R(y) = \sqrt{h^2 + r_g^2 + y^2}. \tag{32}$$

Intermodulation products have the shape of the difference in two hyperbolas.

A comparison of the shapes is illustrated in Fig. 8 for an exemplary two-target scenario and a linear trajectory. The azimuth-dependent target distances are $R1$ and $R2$ and are calculated by (32). Intermodulation products show a range progression proportional to the difference in ToF according to (15). This is also proportional to a difference in range $R2-R1$. Desired range progressions show a positive curvature, and undesired progressions a negative curvature. The amount of the curvature is dependent on the relative change in distance

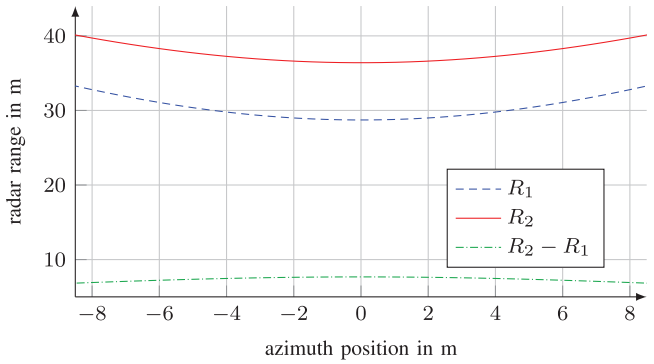

Fig. 8. Theoretical range progression of modulation and intermodulation products along azimuth assuming a linear trajectory for an exemplary two-target scenario.

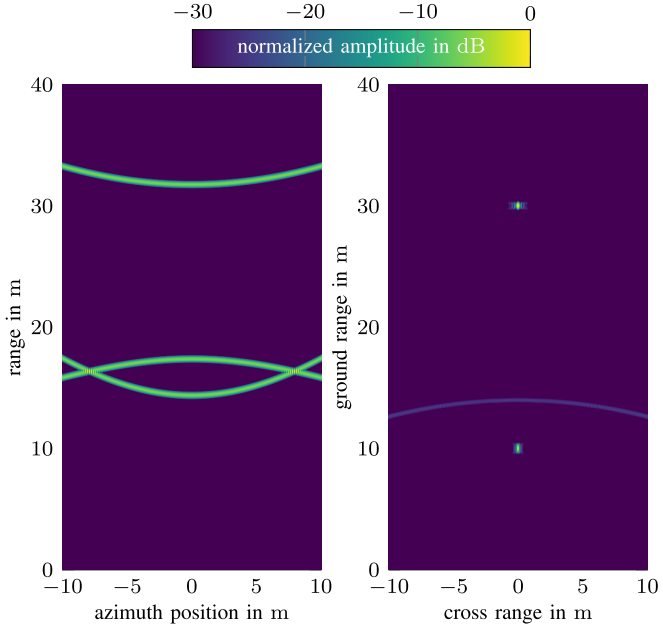

Fig. 9. Simulated range progression (left) and SAR image (right) of a two-target scenario in tandem formation, where the condition of unambiguous imaging is not fulfilled.

along azimuth. Given a high range resolution and small flight altitudes, the progression spans over many range cells and its shape has a great impact on SAR processing. In bistatic geometries, the shape is no longer described by a hyperbola. Still, the curvature behaves similarly.

Fig. 9 shows a simulation of a scenario with two point-like targets, where the condition of unambiguous imaging is not fulfilled, i.e., $\theta > \theta_{\max}$. Tandem formation is considered with h=10 m, $R_{\mathrm{sl}} = 5$ m, a synthetic aperture $L_{\mathrm{sa}} = 20$ m, velocity v=1.5 $\frac{\mathrm{m}}{\mathrm{s}}$, and a measurement rate $f_{\mathrm{prf}} = 100$ Hz. Targets are located at $r_{g,1} = 10$ m and $r_{g,2} = 30$ m. The amplitudes of modulation and intermodulation products are assumed to be equal. The resulting SAR image shows an artifact due to the undesired modulation product in addition to the two desired focused points. However, it is suppressed by 24.7 dB. In a similar simulation with a tomographic formation, a suppression of 24.4 dB is achieved.

3) Amplitude of the Radar Signals: Further suppression of the intermodulation products is possible by adjusting the amplitude of the transmitted signals via sidelink and radar path. As explained in (21), the amplitude of modulation products is proportional to both the sidelink and radar signal amplitude. The intermodulation products are approximately proportional to the square of the radar signal amplitude. This results in a suppression by the factor a_{sup}=a_{sl}/a_{rad}.

To provide a reference for dimensioning the system, $|a_{\mathrm{sup}}|$ is derived in the following. The sidelink received signal power is modeled by the Friis equation for transmission and is given by [58]

$$|a_{\mathrm{sl}}|^2 \propto P_{\mathrm{Rx,sl}} = P_{\mathrm{Tx,sl}} \frac{G_{\mathrm{Tx,sl}} G_{\mathrm{Rx,sl}} \lambda^2}{(4\pi R_{\mathrm{sl}})^2} \tag{33}$$

where $P_{\mathrm{Tx,sl}}$ is the transmit power of the sidelink signal, λ the wavelength of the signal, and $G_{\mathrm{Tx,sl}}$ and $G_{\mathrm{Rx,sl}}$ are the antenna gains of the sidelink transmit and receive antenna, respectively. The radar received signal power is modeled by the bistatic radar equation [60]

$$|a_{\mathrm{rad}}|^2 \propto P_{\mathrm{Rx,rad}} = P_{\mathrm{Tx,rad}} \frac{G_{\mathrm{Tx,rad}} G_{\mathrm{Rx,rad}} \lambda^2 \sigma_{\mathrm{RCS}}}{(4\pi)^3 R_{\mathrm{Tx,rad}}^2 R_{\mathrm{Rx,rad}}^2} \tag{34}$$

where $G_{\mathrm{Tx,rad}}$ and $G_{\mathrm{Rx,rad}}$ are the radar antenna gains and σ_{RCS} is the radar cross section (RCS) of the measured target or scene. Combining (33) and (34) results in

$$|a_{\mathrm{sup}}| = \left| \frac{a_{\mathrm{sl}}}{a_{\mathrm{rad}}} \right| = \sqrt{\frac{4\pi}{\sigma_{\mathrm{RCS}}}} \cdot \sqrt{\frac{P_{\mathrm{Tx,sl}}}{P_{\mathrm{Tx,rad}}}} \cdot \sqrt{\frac{G_{\mathrm{Tx,sl}} G_{\mathrm{Rx,sl}}}{G_{\mathrm{Tx,rad}} G_{\mathrm{Rx,rad}}}} \cdot \frac{R_{\mathrm{Tx,rad}} R_{\mathrm{Rx,rad}}}{R_{\mathrm{sl}}}. \tag{35}$$

This factor can be controlled by adjusting transmit power, antenna gain, or geometry. It represents the amplitude ratio of the modulation and intermodulation products after demodulation. Due to the linearity of the FFT, this applies also after range compression.

D. Influence of Localization Errors

The localization data required for both range offset correction and backprojection may be erroneous. This section aims to analyze the influence of such errors on SAR imaging with the concept introduced in this article.

According to (27), the range-compressed signal is evaluated at the range R_m and the expected phase is calculated for the same range. Thus, R_m is the only variable that determines the value of the range-compressed signal to be summed. R_m is estimated as the distance between the pixel position and the phase center of the transmit or receive antenna. Errors in the estimated antenna position thus translate into range errors in (27). Furthermore, the estimation of the sidelink distance $\hat{R}_{\mathrm{sl}}$ is affected and also translates into a range error.

Two criteria for the maximum tolerable range error can be specified. First, the range error has to be smaller than the size of a range cell. Otherwise, the range-compressed signal would be evaluated at false ranges. This is particularly relevant in systems that use a high bandwidth. Second, the range error directly translates into a phase error, as the phase around a target peak decreases linearly [56]. This affects focusing when applying backprojection. In contrast to the first criterion, this error is dependent on the center frequency and not on the bandwidth. Therefore, the phase error criterion is typically more stringent than the first criterion.

TABLE I
SAR SIMULATION PARAMETERS

Parameter	Symbol	Value
chirp start frequency	f_0	1 GHz
bandwidth	B	800 MHz
chirp duration	T	266.7 µs
chirp rate	K_r	3 THz/s
measurement rate	f_prf	100 Hz
flight altitude above ground	h	10 m
ground range distance	r_g	8 – 12 m
UAV distance	R_sl	5 m
trajectory length	L_sa	20 m
platform speed	v	1.5 m/s
expected ground range resolution	Δr_g	24 – 30 cm
expected cross range resolution	Δr_c	9 cm
number of error vectors per σ_pos	N	1000

There are several types of errors affecting the localization accuracy. GNSS data may drift spatially because of atmospheric effects. This is largely compensated for if real-time kinematic (RTK) GNSS is deployed. The estimation of the expected phase applied in (27) requires the precise knowledge of the phase center of the antenna. Inaccuracies may cause offsets in all spatial dimensions.

Errors in the estimation of the heading also translate into spatial offsets. If the center of rotation is assumed to be known without errors, the coordinate transformation to the phase center of the antennas is still erroneous if the heading data are incorrect. This is because the local lever arm vector (x_l, y_l, z_l) has to be rotated with the knowledge of the heading data. In the system under consideration, the component $x_l = 25$ cm is the dominant vector component. A heading offset $\Delta\varphi$ would result in a corresponding spatial displacement

$$\Delta x = x_l\,(1 - \cos\Delta\varphi)\,. \tag{36}$$

For exemplary heading errors $\Delta\varphi = 5°$, 10°, and 20° and considering the limiting case where the heading offset results in twice a range offset, the resulting range errors are δR=2Δx = 0.2, 0.8, and 3.0 cm.

Assuming a maximum tolerable range offset $\lambda/10 = 0.2$, 0.8, and 3.0 cm as discussed in Section II-C, the maximum tolerable heading offset results in

$$\Delta\varphi_\mathrm{max} = \arccos\left(1 - \frac{\lambda}{20x_l}\right) = 16°. \tag{37}$$

In the following analysis, offsets in x, y, and z are assumed without further specification of their source. Normal distributed independent error vectors in each dimension are generated and low-pass-filtered by applying a moving average with length M_f along the single measurements m to prevent discontinuities along the trajectory. The initial standard deviation is set to $(M_f)^{1/2}\sigma_\mathrm{pos}$ so that after applying the moving average filter, the resulting standard deviation is σ_pos. Random offsets are then added to each of the axes, assuming the errors on Tx and Rx are uncorrelated.

SAR simulations are performed with the parameters given in Table I and error vectors with differing standard deviations σ_pos. Four point-like targets are considered and N=1000 runs per value of σ_pos are performed. Fig. 10 shows four exemplary SAR images for a bistatic tandem formation.

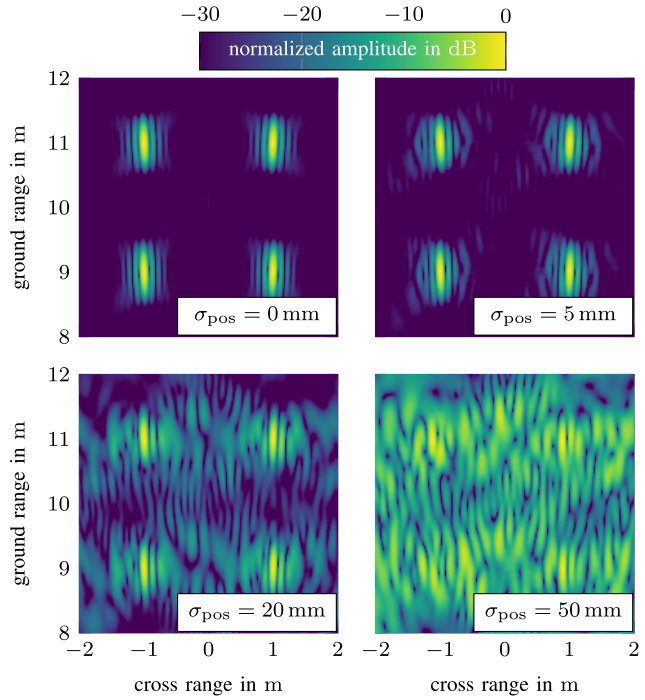

Fig. 10. Simulated SAR images in bistatic tandem formation and a four-target scenario for localization error vectors with different standard deviations σ_pos.

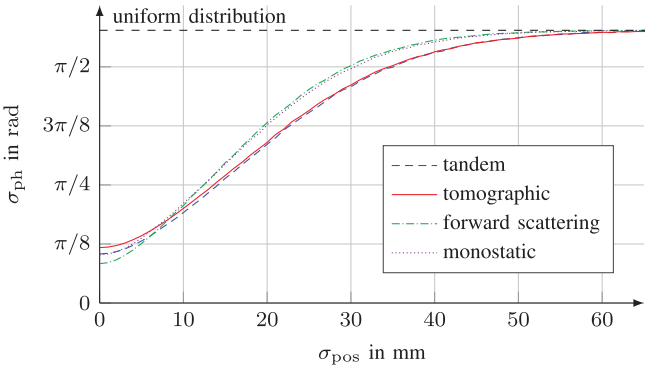

Fig. 11. Simulated influence of the standard deviation of the localization error on the phase distribution before summation over m.

The targets appear focused for $\sigma_\mathrm{pos} \leq 20$ mm while the clutter level increases with increasing standard deviation of the error vector. SAR images itself, however, provide only a visual estimation of the error impact. To allow a quantitative analysis, the phase distribution of a pixel value at a target position is considered before summing along m. This distribution allows a prediction of how well a target is focused the SAR image [61]. Uniform phase distribution results in no focusing, while a constant phase value for all m causes the maximum possible pixel amplitude.

SAR simulations with the same parameters are performed for the three formations introduced in Section II-D and for a monostatic geometry. Fig. 11 shows the standard deviation of the phase σ_ph of all pixel phases at the target positions before summation. The minimum standard deviation of around $\pi/8$ is due to the presence of multiple targets and their impact on each

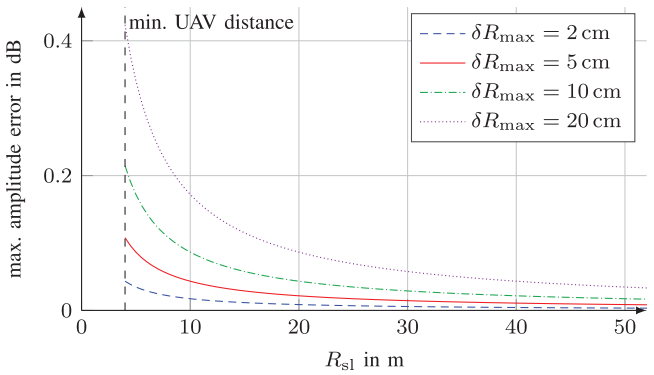

Fig. 12. Amplitude error due to erroneous sidelink distance estimation after correction with (33).

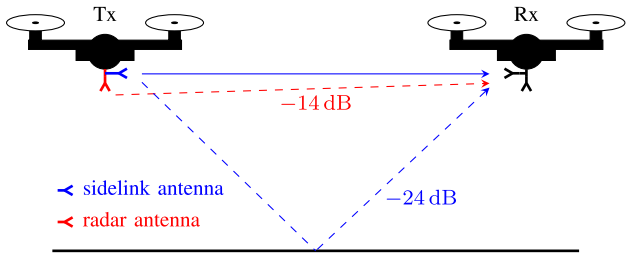

Fig. 13. Desired (——) and relevant undesired (- - -) components at the sidelink Rx antenna with attenuation values due to the antenna pattern from the configuration used in Section V.

other. An increase in the standard deviation can be observed for a decreased localization accuracy. At approximately 50 mm, a uniform distribution is reached, resulting in no focusing of the targets.

For lower accuracies, tandem and tomographic formations perform slightly better than monostatic and forward scattering. The reason for this is that in a bistatic geometry, i.e., tandem and tomographic, differential parts of the error vector can cancel each other out, while errors in a monostatic geometry always impact both transmit and receive path in the same direction.

E. Influence of Amplitude Deviations

In contrast to synchronization methods, where local oscillators at each node are synchronized, the reference signal in this concept is transmitted via a wireless link. Hence, the amplitude of this signal is not constant along the single acquisitions of an SAR measurement.

The received power of the sidelink signal used as reference is given by (33). If the heading of the UAV varies, the antenna gain changes, as transmission in boresight can be no longer assumed. However, this effect is small in a constant flight formation and can be corrected if necessary, as the heading should be known anyway for precise localization of the antenna phase centers.

Fluctuations in range, i.e., in R_{sl}, are more severe. In close formations, a change in a few meters can have a major impact on the signal amplitude. However, these changes can be modeled using the precise knowledge of R_{sl} and (33). Then, the amplitude deviation can be corrected.

Assuming a maximum error of $\delta R_{\max}$ in the estimation of R_{sl}, the amplitude error after the correction is analyzed and illustrated in Fig. 12. For a minimum UAV distance of 4 m and an error $\delta R_{\max} = 2$ cm, the amplitude error is below 0.1 dB. The value of $\delta R_{\max}$ was chosen according to the analysis in Section IV-D. Thus, no loss in performance is to be expected.

F. Influence of the Antenna Pattern

The previous explanations assumed that only one sidelink signal and one radar signal for each target is present at the receiver. In practice, sidelobes in the antenna pattern may cause additional signal components. The sidelink signal is received not only via the direct path but also via the specular ground reflection. Fig. 13 illustrates the relevant desired and undesired signals that are received by the Rx sidelink antenna. The reflected sidelink signal, however, is suppressed due to three factors.

First, the sidelobes that may lead to these additional paths are usually low compared with the main beam. In the considered system, the radiation pattern of the sidelink antenna in the direction of the specular reflection is 12 dB. This value affects both Tx and Rx and thus results in an attenuation of 24 dB due to the pattern. Second, the ground path is generally longer than the direct path. Hence, the free-space path loss is larger and the signal is further suppressed. The path length of the specular reflection path is given by

$$R_{\text{spec}} = R_{\text{sl}} \sqrt{1 + \frac{4h^2}{R_{\text{sl}}^2}}. \tag{38}$$

In most practical scenarios that use a side-looking geometry, this path length is both significantly larger than the sidelink path and lower than the minimum expected radar return. In the considered geometry provided in Section V-C, (38) yields $R_{\text{spec}} = 10.0$ m. This is 5.7 m more than the sidelink, even in a low-altitude scenario such as the one considered here. Third, not all the power is reflected from the ground toward the receiver. The amount of the reflected power can be determined using Fresnel's equations. Furthermore, in a side-looking scenario, this signal appears at a range, which is typically lower than all ranges considered in the backprojection algorithm and thus does not degrade the imaging quality.

Moreover, the sidelink signal may also be transmitted via the sidelobes of the radar antennas, as illustrated in Fig. 13. By designing the pattern to have low sidelobes orthogonal to the boresight and carefully positioning the antennas, the power of this signal component can be effectively suppressed. Assuming the same transmit power, the ratio of the sidelink and direct radar signal equals the attenuation due to the pattern of the radar antenna in sidelink direction. In the considered case, the direct radar signal is 14 dB lower in power than the desired sidelink signal. However, the difference in path length is only 8 cm, so both the signals are in the same range cell. The same holds for the signal transmitted by the sidelink antenna and received by the radar antenna.

V. Experimental Verification

The concept is demonstrated via bistatic radar measurements. In the first part of this section, the system used as transmit and receive node is presented. Static measurements

TABLE II
RADAR PARAMETERS OF THE MEASUREMENT SYSTEM

Parameter	Symbol	Value
chirp start frequency	f_0	1.2 GHz
bandwidth	B	409.6 MHz
chirp duration	T	136.5 µs
chirp rate	K_r	3 THz/s
measurement rate	f_{prf}	100 Hz
ADC sampling rate (Rx)	f_s	4.096 GS/s

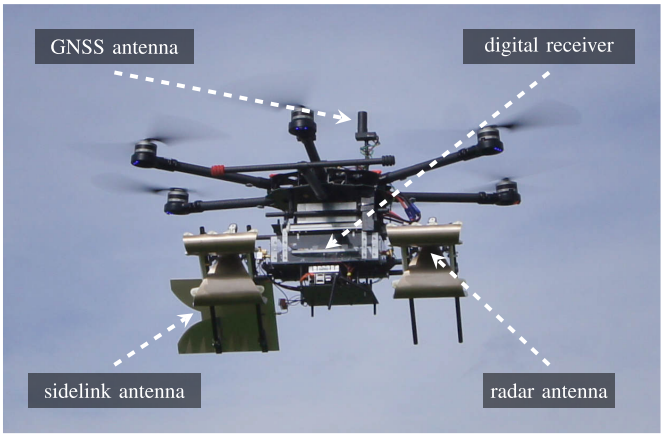

Fig. 14. Photograph of the UAV carrying the digital receiver system as used in the experiment.

are carried out to validate the signal processing described in Section III and prove the coherency achieved in the concept. A UAV-based bistatic measurement demonstrates the application of the concept for SAR imaging of objects in a realistic scenario based on the results of Section IV.

A. System

A radar with FMCW modulation operates as transmitting node. The signal parameters are given in Table II. The transmit signal is split into two paths, the radar and the sidelink path, each with a dedicated antenna.

The digital receiver consists of the same antennas for radar and sidelink path, an RFSoC with fast ADCs to sample the RF signal, and a memory interface to SSD storage devices. The sampling rate at the receiver ADC is given in Table II.

Digital demodulation is performed with a carrier frequency of $f_c = 1.2$ GHz and a resulting small carrier frequency offset compared with the transmit signal is corrected digitally. A decimation by a factor of 4 is applied after sampling, resulting in a sampling rate of f_s =1.024 $\frac{\text{GS}}{\text{s}}$ for the signals used in postprocessing. These steps are only done for practical reasons and do not affect the system concept. Signal processing is done offline after data acquisition.

For the SAR experiment, the transmit and receive systems are mounted on a multicopter each, shown in Fig. 14. A TEM horn antenna is used for the radar path [62], a Vivaldi antenna for the sidelink path.

GNSS data are used for both generating a common time reference and providing the localization data necessary for SAR processing. A commercially available dual-band GNSS receiver combined with RTK data from a base station is used for this purpose. For a subcentimeter localization accuracy, these data are fused with data from an onboard inertial measurement unit [63].

TABLE III
POSITIONS WITHIN STATIC SCENE

Object	x position	y position	Range
Tx node	0 m	0 m	
Rx node	1.10 m	0 m	
target 1 (metal cylinder)	−0.65 m	2.29 m	2.63 m
target 2 (metal cylinder)	0.79 m	4.39 m	4.43 m

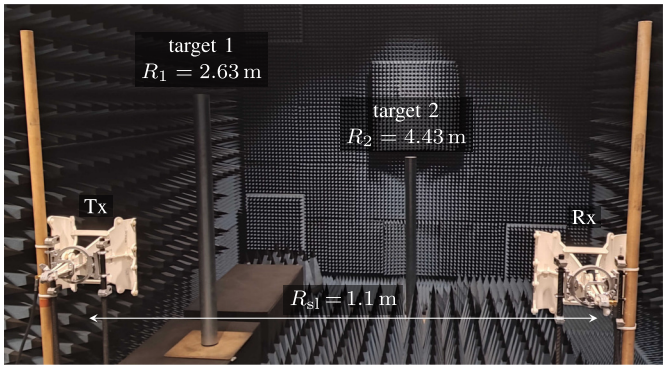

Fig. 15. Photograph of the static measurement setup consisting of a two-target scenario and spatially separated transmitter (Tx) and receiver (Rx) nodes with one-way radar ranges R_1 and R_2.

B. Static Radar Measurement

Two metallic cylindric targets are placed inside an anechoic chamber to validate the concept of digital demodulation from Section III and to analyze the coherency. Fig. 15 shows the experimental setup indicating the positions of Tx and Rx nodes and both the targets. The positions of the Tx and Rx nodes and both the targets are provided in Table III.

The sidelink relies on a cable between Tx and Rx nodes. This prevents multiple reflections inside the chamber, which are more severe in an indoor scenario compared with the subsequent free-space experiment. Taking into account the permittivity within the cable, the sidelink distance is $R_{sl} = 1.1$ m. Radar and sidelink signal are stored separately, digitally combined, and squared for demodulation. An analog combination would provide the same result, and digital combination was only performed to check the data before. To reduce the sidelobe level, a Hann window is applied and range compression is performed. A series of 150 measurements are then combined coherently by averaging them and normalizing the resulting data to the maximum. The resulting range-compressed signal is shown in Fig. 16.

The peak location after correcting the estimated sidelink range offset $\hat{R}_{sl}$ is consistent with the geometrically expected ranges indicated by vertical dashed lines. The intermodulation product at $R{=}R_2 - R_1 + R_{sl}/2 = 2.35$ m is not visible, as the amplitude of the modulation products is significantly larger. Note that the range-compressed signal in Fig. 16 shows the one-way radar range.

Phase coherence is crucial for SAR processing. Thus, the phase of the range-compressed signal at the target positions is

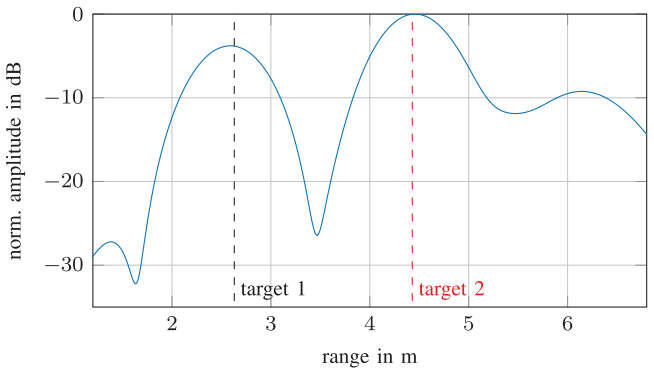

Fig. 16. Range-compressed signal of the static measurement of the two-target scenario shown in Fig. 15 with ground-truth ranges indicated by dashed lines.

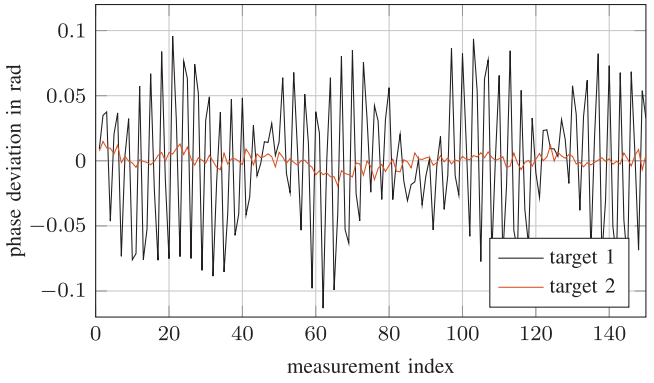

Fig. 17. Phase deviation relative to the mean phase at the target peak maximums of the range-compressed data in Fig. 16.

considered before summation of the 150 single measurements. The resulting phase deviations relative to the mean phase are shown in Fig. 17.

A measure of the coherence that allows predictions on the resulting SAR image after applying the backprojection algorithm is the coherence factor [64]

$$\Gamma_{\mathrm{cf}} = \frac{\left|\sum_{m=1}^{M} S_{B,m}(R_m)\right|^2}{M \cdot \sum_{m=1}^{M} \left|S_{B,m}(R_m)\right|^2} \tag{39}$$

where M is the number of single measurements that are processed jointly. By comparing coherent and incoherent summation of complex values, the impact of phase deviations over repeated measurements can be measured. In this context, $\Gamma_{\mathrm{cf}} = 0$ means destructive summation, $\Gamma_{\mathrm{cf}}=(1/M)$ incoherent summation, i.e., no usable phase information, and $\Gamma_{\mathrm{cf}} = 1$ coherent summation.

Since backprojection uses the coherent sum to focus targets, a direct correlation between coherence factor and backprojection exists. Ideally, the phase in a static measurement is constant. Deviations in the phase along a series of measurements can thus be considered as performance limit for coherent processing.

For the targets, the coherence factor is determined as $\Gamma_{\mathrm{cf},1} = 0.997$ and $\Gamma_{\mathrm{cf},2} = 1.000$, respectively. Thus, no perceptible loss in performance is expected when applying the concept for SAR imaging. This is analyzed in the following by a bistatic SAR experiment.

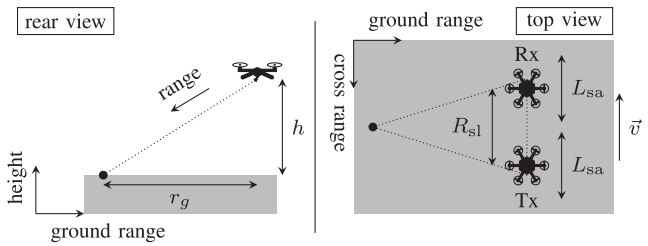

Fig. 18. Illustration of the measurement geometry of the bistatic UAV-based SAR experiment in tandem formation with flight direction $\vec{v}$.

TABLE IV
UAV-BASED MEASUREMENT GEOMETRY

Parameter	Symbol	Value
flight altitude above ground	h	4.5 m
ground range distance	r_{g}	11 m
UAV distance	R_{sl}	4.3 m
trajectory length	L_{sa}	6.3 m
depression angle	α	45°
platform speed	v	0.5 m/s
measurement rate	f_{prf}	10 Hz
expected ground range resolution	Δr_{g}	57 cm
expected cross range resolution	Δr_{c}	17 cm

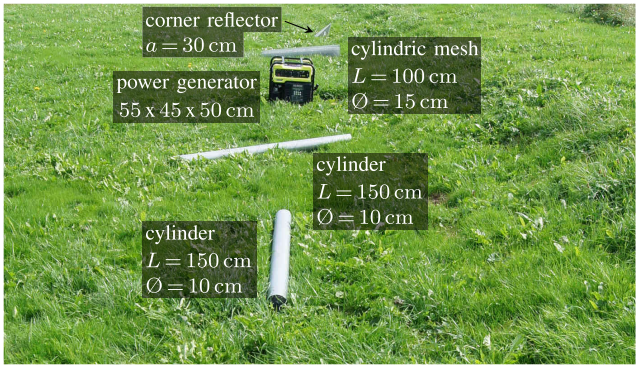

Fig. 19. Photograph of the measured scene with the extended target and surrounding consisting of multiple metallic targets and a grass-covered mound on the right behind the targets. Edge length a of the corner reflector as well as length L and diameter $\varnothing$ of the cylinders are indicated.

C. UAV-Based SAR Measurement

After proving the phase stability and coherent nature of the concept, a UAV-based bistatic SAR measurement is carried out. This experiment aims to verify the SAR processing explained in Section IV.

The UAVs fly in tandem formation with the receiving system in the front. A schematic representation of the measurement geometry is displayed in Fig. 18, and the related parameters are given in Table IV. The radar parameters are the same as in the static measurement and are presented in Table II. In contrast to the previous evaluation, a measurement rate of 10 Hz is used. The antennas are mounted in a vertically polarized configuration.

The measured scene consists of a grass surface with several metallic objects, as shown in Fig. 19. A grass-covered mound is located behind the targets at a slightly larger range. The positions and orientations are denoted in Table V. For the following analysis, a power generator as an exemplary extended

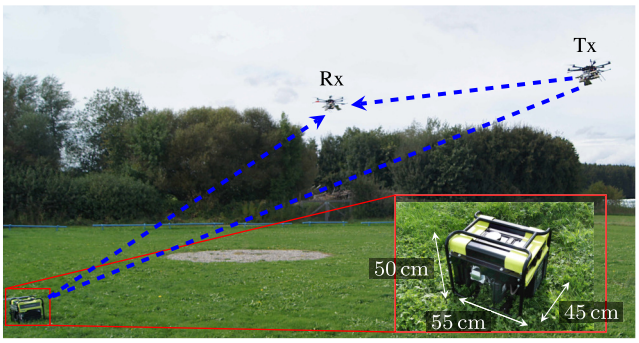

Fig. 20. Photograph of the UAVs and the measurement setup during the bistatic SAR experiment.

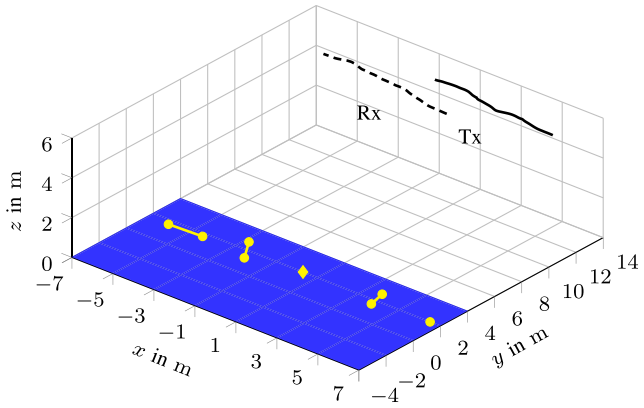

Fig. 21. Measurement geometry for the bistatic SAR experiment with transmit (——) and receive nodes (- - -) as well as the pixel grid (■) and positions of the evaluated (♦) and additional targets (●) indicated.

TABLE V
POSITIONS AND ORIENTATION OF OBJECTS WITHIN THE SCENE

Object	Cross range position	Ground range position	Orientation (rel. to x axis)
metal cylinder	−5.6 m	1.6 m	4°
metal cylinder	−2.8 m	2.0 m	−62°
power generator	0.0 m	2.0 m	6°
cylindric wire mesh	3.5 m	2.2 m	−81°
corner reflector	6.2 m	2.0 m	≈ 0°
grass mound (height: 0.5 m)	−7 . . . 7 m	−1 . . . 1 m	7°

object is considered. Fig. 20 shows a photograph taken during the acquisition with both the UAVs and the dimensions of the measured target. An illustration of the trajectory for both the transmit and receive nodes, the evaluated area, and the target positions is given in Fig. 21. The dimensions of the power generator are indicated in Fig. 20.

Digital demodulation and range compression are performed following the signal processing described in Section III. A Hann window is applied before range compression to suppress sidelobes. SAR processing is performed by applying the backprojection algorithm described in Section IV. The expected resolutions in ground and cross range direction can be calculated for point-like targets and a monostatic geometry [65]. The resulting values are listed in Table IV.

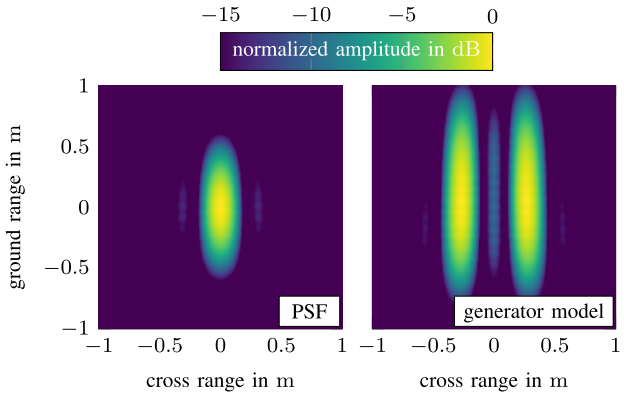

Fig. 22. Simulated PSF of the measurement system and geometry (left) and simulated SAR image of a simplified model of the power generator (right).

TABLE VI
RESOLUTIONS IN CROSS RANGE AND GROUND RANGE

Evaluation	Δr_c	Δr_g
theory	17 cm	57 cm
simulation (PSF)	19 cm	58 cm
simulation (generator model)	17 cm	103 cm
measured SAR image	19 cm	83 cm

With the results from Section IV-C1 and Fig. 7, the unambiguous elevation angle can be determined to $\theta_{\max} = 61°$. This results in an unambiguous swath width of $r_{g,\max} = 8.12$ m. Thus, the first condition to suppress intermodulation products is not fulfilled because of the low flight altitude, close UAV distance, and flat elevation angle. However, the second condition explained in Section IV-C2 is met because of the extreme close-range geometry and high radar resolution.

The third condition derived in Section IV-C3 can be verified by estimating the amplitude ratio $|a_{\text{sup}}|$ between modulation and intermodulation products from (35). The sidelink transmit power is 20 dB lower than the radar transmit power to ensure a high dynamic range at the receiver. The antenna gains are G_{sl}=8 dBi and G_{rad}=6 dBi for sidelink and radar path, respectively. Transmit and receive antennas are identical.

The RCS of the power generator can only be estimated roughly because of its complex shape. The target is modeled as a rectangular plate that represents the front surface of the object. This is done because of the flat elevation angle of approximately 22° measured from ground. Combining the geometric parameters in Table IV and the derivation by Jackson et al. [66], this results in σ_{RCS}=−2.3 dBsm. Calculating (35), a further suppression of $|a_{\text{sup}}| = 26$ dB is achieved. However, this is only an estimate to show the order of magnitude of the suppression.

A simulation of the point-spread function (PSF) was performed with the system and geometric parameters in Tables II and IV. Furthermore, a simplified model of the power generator was simulated, where the vertical metal edges were modeled as infinitesimally thin rods. Due to the vertical polarization used, these are expected to contribute most to the radar return of the object. The results of both the simulations are depicted in Fig. 22. The 3 dB-resolutions in cross range and ground range are provided in Table VI.

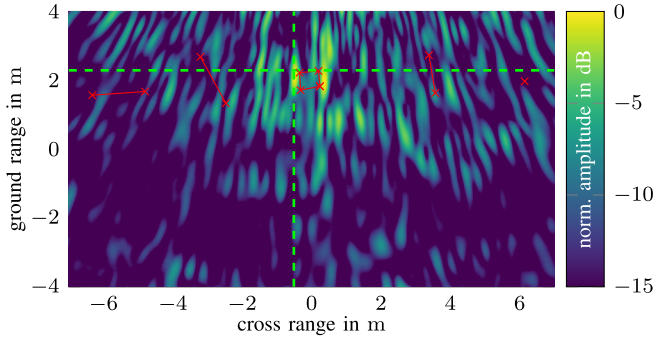

Fig. 23. Measured bistatic SAR image of the scene shown in Fig. 20 with two UAVs in tandem formation. The considered target is marked by a red box, other objects by red lines and marks. Cuts along cross and ground range are marked by green dashed lines.

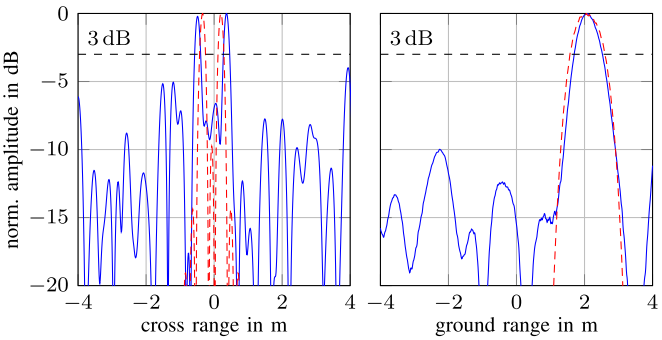

Fig. 24. Cuts through the bistatic SAR image shown in Fig. 23 along cross and ground range for measured (——) and simulated (- - -) data.

Fig. 23 shows the measured bistatic SAR image of the scene. The ground-truth position of the power generator is marked with the red box, and additional objects in the surrounding area with red lines and marks.

Despite the high-clutter environment caused by the uneven surface topology and returns by the grass itself as shown in Fig. 19, a focusing of the extended object is clearly visible. The presence of two focused shapes corresponds to the simulated generator model in Fig. 22. Returns from the other targets cannot be distinguished from the clutter present in the SAR image. The cylinders are placed flat on the ground, thus the backscattered power is expected to be small. In addition, the return of the corner reflector is expected to be weak because the signal is scattered back toward the incident direction, i.e., the UAV with the transmitting node. Clutter in the SAR image may be due to returns from the grass or from a small hill behind the targets. Moreover, multiple reflections and different scattering centers of extended objects can degrade the focusing and broaden the target peak.

To further analyze the performance of the concept, cuts along ground and cross range are evaluated. The results are displayed in Fig. 24. The measured 3 dB-resolution is indicated in the cuts and denoted in Table VI. The simulation results of the generator model are used as reference. Both along cross range and ground range, the measured SAR data in the vicinity of the target closely match the simulated data. The proposed concept ensures coherency not only within a single radar acquisition but also across all the measurements along the trajectory. This is validated by the measured cross range resolution, which shows good agreement with the theoretically achievable resolution. Due to the high resolution, the two metal rods of the power generator are distinguishable in the SAR image. In the ground range direction, the measured resolution is between the expected value for a point-like target and the simulated result for the generator model. The deviation may result from the limitations of the simplified model, which does not fully capture the complexity of the real scenario.

VI. Conclusion

Multistatic SAR on spatially separated independent platforms places high demands on the coherency in time, frequency, and phase. For conventional approaches, this often results in a need for high synchronization accuracy. With the concept introduced in this work, timing requirements are reduced by several orders of magnitude, enabling high-resolution UAV-based multistatic SAR processing. Digital receive-only nodes allow scalability to a large swarm of UAVs and thus applications such as single-pass tomography.

By receiving the radar signal via two paths, sampling the RF signal, and squaring the combined signal, coherent demodulation is performed. The required synchronization accuracy is translated into localization accuracy of the nodes, which is necessary for UAV-based SAR imaging anyway. This allows for multistatic SAR imaging, where phase coherence is crucial.

After explaining the digital demodulation and SAR processing using a model of the received signal, the influence of intermodulation products, localization errors, and amplitude deviation were considered. Each of these aspects results in limitations that are not more restrictive than in a monostatic UAV-based scenario.

The concept was verified by analyzing static measurements in an anechoic chamber and carrying out an experiment with two UAVs in a realistic scenario. With that, the coherent processing was proven and a high-resolution bistatic SAR image could be generated.

Appendix
Derivation of the Bistatic Unambiguous Range

Analogous to the derivation of the monostatic unambiguous range in Section IV-C1, the bistatic unambiguous range for the tandem formation is derived. The condition in (29) that the difference of $R_{\max}$ and $R_{\min}$ has to be smaller or equal to $R_{\min}$ is generally valid. Similar to the derivation in Section IV-C1, one-way radar ranges are considered.

The minimum range in the bistatic tandem scenario is represented by the specular ground reflection and can be expressed by

$$R_{\min} = \sqrt{\frac{R_{\mathrm{sl}}^2}{4} + h^2}. \tag{40}$$

The maximum range is limited by the maximum elevation angle $\theta_{\max}$ as explained in the monostatic case. Taking into account the distance R_{sl} between transmit and receive node, the following value is obtained

$$R_{\max} = \sqrt{\frac{R_{\mathrm{sl}}^2}{4} + \frac{h^2}{\cos\left(\theta_{\max}\right)^2}}. \tag{41}$$

The condition in (29) yields

$$\sqrt{\frac{R_{\mathrm{sl}}^2}{4}+\frac{h^2}{\cos(\theta_{\max})^2}}-\sqrt{\frac{R_{\mathrm{sl}}^2}{4}+h^2}\overset{!}{\leq}\sqrt{\frac{R_{\mathrm{sl}}^2}{4}+h^2}. \tag{42}$$

Rearranging the equation yields

$$\begin{aligned}\sqrt{\frac{R_{\mathrm{sl}}^2}{4}+\frac{h^2}{\cos(\theta_{\max})^2}}&\leq 2\sqrt{\frac{R_{\mathrm{sl}}^2}{4}+h^2}\\ \frac{R_{\mathrm{sl}}^2}{4}+\frac{h^2}{\cos(\theta_{\max})^2}&\leq 4\left(\frac{R_{\mathrm{sl}}^2}{4}+h^2\right)\\ \frac{h^2}{\cos(\theta_{\max})^2}&\leq \frac{3R_{\mathrm{sl}}^2}{4}+4h^2\\ \frac{\cos(\theta_{\max})^2}{h^2}&\geq \frac{1}{\frac{3R_{\mathrm{sl}}^2}{4}+4h^2}\\ \cos(\theta_{\max})&\geq \frac{2h}{\sqrt{3R_{\mathrm{sl}}^2+16h^2}}.\end{aligned} \tag{43}$$

With (30), the maximum unambiguous swath width can be calculated. Using the relation

$$\tan(\arccos(x))=\frac{\sqrt{1-x^2}}{x} \tag{44}$$

the maximum unambiguous swath width results in

$$\begin{aligned}r_{g,\max}&=h\sqrt{1-\left(\frac{2h}{\sqrt{3R_{\mathrm{sl}}^2+16h^2}}\right)^2}\left(\frac{2h}{\sqrt{3R_{\mathrm{sl}}^2+16h^2}}\right)^{-1}\\ &=\frac{1}{2}\sqrt{\frac{3R_{\mathrm{sl}}^2+12h^2}{3R_{\mathrm{sl}}^2+16h^2}}\sqrt{3R_{\mathrm{sl}}^2+16h^2}\\ &=\frac{1}{2}\sqrt{3R_{\mathrm{sl}}^2+12h^2}.\end{aligned} \tag{45}$$

Note that for $R_{\mathrm{sl}}=0$, the monostatic scenario is represented as explained in Section IV-C1.

ACKNOWLEDGMENT

The authors would like to thank the anonymous reviewers for their valuable comments, which led to the correction of a signal processing issue and improved agreement between the experimental results and the theoretical predictions.

REFERENCES

[1] P. Hugler, F. Roos, M. Schartel, M. Geiger, and C. Waldschmidt, "Radar taking off: New capabilities for UAVs," *IEEE Microw. Mag.*, vol. 19, no. 7, pp. 43–53, Nov. 2018.

[2] I. Ullmann et al., "Towards detecting climate change effects with UAV-borne imaging radars," *IEEE J. Microw.*, vol. 4, no. 4, pp. 1–13, Oct. 2024.

[3] S. Prager, G. Sexstone, D. McGrath, J. Fulton, and M. Moghaddam, "Snow depth retrieval with an autonomous UAV-mounted software-defined radar," *IEEE Trans. Geosci. Remote Sens.*, vol. 60, 2022, Art. no. 5104816.

[4] T. O. Teisberg, D. M. Schroeder, A. L. Broome, F. Lurie, and D. Woo, "Development of a uav-borne pulsed ICE-penetrating radar system," in *Proc. IEEE Int. Geosci. Remote Sens. Symp.*, Jul. 2022, pp. 7405–7408.

[5] A. Grathwohl, P. Hinz, R. Burr, M. Steiner, and C. Waldschmidt, "Experimental study on the detection of avalanche victims using an airborne ground penetrating synthetic aperture radar," in *Proc. IEEE Radar Conf.*, May 2021, pp. 1–6.

[6] P. Stockel, P. Wallrath, R. Herschel, and N. Pohl, "Detection and monitoring of people in collapsed buildings using a rotating radar on a UAV," *IEEE Trans. Radar Syst.*, vol. 2, pp. 13–23, 2024.

[7] M. Schartel, R. Burr, W. Mayer, N. Docci, and C. Waldschmidt, "UAV-based ground penetrating synthetic aperture radar," in *IEEE MTT-S Int. Microw. Symp. Dig.*, Apr. 2018, pp. 1–4.

[8] O. Frey, C. L. Werner, and R. Coscione, "Car-borne and UAV-borne mobile mapping of surface displacements with a compact repeat-pass interferometric SAR system at L-band," in *Proc. IEEE Int. Geosci. Remote Sens. Symp.*, Jul. 2019, pp. 274–277.

[9] V. Mustieles-Perez et al., "Experimental demonstration of UAV-based ultra-wideband multi-baseline SAR interferometry," in *Proc. Eur. Conf. Synth. Aperture Radar (EUSAR)*, 2024, pp. 1156–1161.

[10] L. Miccinesi, A. Beni, L. Bigazzi, and M. Pieraccini, "Synthetic aperture radar aboard an unmanned aerial system for detecting foreign object debris on airport runways," *IEEE Access*, vol. 12, pp. 106735–106743, 2024.

[11] J. Svedin, A. Bernland, A. Gustafsson, E. Claar, and J. Luong, "Small UAV-based SAR system using low-cost radar, position, and attitude sensors with onboard imaging capability," *Int. J. Microw. Wireless Technol.*, vol. 13, no. 6, pp. 602–613, Mar. 2021.

[12] A. Grathwohl et al., "Taking a look beneath the surface: Multicopter UAV-based ground-penetrating imaging radars," *IEEE Microw. Mag.*, vol. 23, no. 10, pp. 32–46, Oct. 2022.

[13] Y. Á. López, M. García-Fernández, G. Álvarez-Narciandi, and F. L. Andrés, "Unmanned aerial vehicle-based ground-penetrating radar systems: A review," *IEEE Geosci. Remote Sens. Mag.*, vol. 10, no. 2, pp. 66–86, Jun. 2022.

[14] F. Brigui, S. Angelliaume, N. Castet, X. Dupuis, and P. Martineau, "SAR-light–first SAR images from the new onera SAR sensor on UAV platform," in *Proc. IEEE Int. Geosci. Remote Sens. Symp.*, Jul. 2022, pp. 7721–7724.

[15] A. Bekar, M. Antoniou, and C. J. Baker, "Low-cost, high-resolution, drone-borne SAR imaging," *IEEE Trans. Geosci. Remote Sens.*, vol. 60, 2022, Art. no. 5208811.

[16] G. Krieger et al., "TanDEM-X: A satellite formation for high-resolution SAR interferometry," *IEEE Trans. Geosci. Remote Sens.*, vol. 45, no. 11, pp. 3317–3341, Nov. 2007.

[17] A. Moreira et al., "Tandem-L: A highly innovative bistatic SAR mission for global observation of dynamic processes on the Earth's surface," *IEEE Geosci. Remote Sens. Mag.*, vol. 3, no. 2, pp. 8–23, Jun. 2015.

[18] J. L. Garrison, A. Komjathy, V. U. Zavorotny, and S. J. Katzberg, "Wind speed measurement using forward scattered GPS signals," *IEEE Trans. Geosci. Remote Sens.*, vol. 40, no. 1, pp. 50–65, Jan. 2002.

[19] V. Zavorotny et al., "Seasonal polarimetric measurements of soil moisture using tower-based GPS bistatic radar," in *Proc. IEEE Int. Geosci. Remote Sens. Symp.*, vol. 2, Jul. 2003, pp. 781–783.

[20] N. Pierdicca, L. Pulvirenti, F. Ticconi, and M. Brogioni, "Radar bistatic configurations for soil moisture retrieval: A simulation study," *IEEE Trans. Geosci. Remote Sens.*, vol. 46, no. 10, pp. 3252–3264, Oct. 2008.

[21] M. Stefko, P. Bernhard, O. Frey, and I. Hajnsek, "Polarimetric analysis of biseasonal monostatic and bistatic radar observations of a glacier accumulation zone at Ku-band," *IEEE J. Sel. Topics Appl. Earth Observ. Remote Sens.*, vol. 17, pp. 9706–9727, 2024.

[22] M. Pieraccini, L. Miccinesi, and N. Rojhani, "A GBSAR operating in monostatic and bistatic modalities for retrieving the displacement vector," *IEEE Geosci. Remote Sens. Lett.*, vol. 14, no. 9, pp. 1494–1498, Sep. 2017.

[23] Y. Wang et al., "First demonstration of single-pass distributed SAR tomographic imaging with a P-Band UAV SAR prototype," *IEEE Trans. Geosci. Remote Sens.*, vol. 60, 2022, Art. no. 5238618.

[24] J. Kanz, C. Bonfert, R. Riekenbrauck, and C. Waldschmidt, "Bistatic UAV-based repeater SAR for 3D object localization," in *Proc. Eur. Conf. Synth. Aperture Radar (EUSAR)*, Apr. 2024, pp. 1144–1149.

[25] O. Reyhanigalangashi et al., "Ultra-wideband bistatic radar measurements of snow," *IEEE J. Microw.*, vol. 4, no. 4, pp. 894–905, Oct. 2024.

[26] D.-H. Shin, D.-H. Jung, D.-C. Kim, J.-W. Ham, and S.-O. Park, "A distributed FMCW radar system based on fiber-optic links for small drone detection," *IEEE Trans. Instrum. Meas.*, vol. 66, no. 2, pp. 340–347, Feb. 2017.

[27] A. Durr et al., "High-resolution 160-GHz imaging MIMO radar using MMICs with on-chip frequency synthesizers," *IEEE Trans. Microw. Theory Techn.*, vol. 67, no. 9, pp. 3897–3907, Sep. 2019.

[28] A. Durr, D. Bohm, D. Schwarz, S. Hafner, R. Thoma, and C. Waldschmidt, "Coherent measurements of a multistatic MIMO radar network with phase noise optimized non-coherent signal synthesis," *IEEE J. Microw.*, vol. 2, no. 2, pp. 239–252, Apr. 2022.

[29] M. Stefko, O. Frey, C. Werner, and I. Hajnsek, "Calibration and operation of a bistatic real-aperture polarimetric-interferometric Ku-band radar," *IEEE Trans. Geosci. Remote Sens.*, vol. 60, 2022, Art. no. 5106719.
[30] J. M. Merlo, S. Wagner, J. Lancaster, and J. A. Nanzer, "Fully wireless coherent distributed phased array system for networked radar applications," *IEEE Microw. Wireless Technol. Lett.*, vol. 34, no. 6, pp. 837–840, Jun. 2024.
[31] V. Janoudi, P. Schoeder, T. Grebner, N. Appenrodt, J. Dickmann, and C. Waldschmidt, "Signal model for coherent processing of uncoupled and low frequency coupled MIMO radar networks," *IEEE J. Microw.*, vol. 4, no. 1, pp. 69–85, Jan. 2024.
[32] M. Gottinger, P. Gulden, and M. Vossiek, "Coherent signal processing for loosely coupled bistatic radar," *IEEE Trans. Aerosp. Electron. Syst.*, vol. 57, no. 3, pp. 1855–1871, Jun. 2021.
[33] P. Fenske, T. Koegel, R. Ghasemi, and M. Vossiek, "Constellation estimation, coherent signal processing, and multiperspective imaging in an uncoupled bistatic cooperative radar network," *IEEE J. Microw.*, vol. 4, no. 3, pp. 486–500, Jul. 2024.
[34] R. Ghasemi, P. Fenske, T. Koegel, M. Hehn, I. Ullmann, and M. Vossiek, "Ultrahigh-performance radio frequency system-on-chip implementation of a Kalman filter-based high-precision time and frequency synchronization for networked integrated sensing and communication systems," *IEEE Open J. Instrum. Meas.*, vol. 4, pp. 1–15, Jun. 2025.
[35] A. Frischen, J. Hasch, and C. Waldschmidt, "A cooperative MIMO radar network using highly integrated FMCW radar sensors," *IEEE Trans. Microw. Theory Techn.*, vol. 65, no. 4, pp. 1355–1366, Apr. 2017.
[36] A. Frischen, G. Hakobyan, and C. Waldschmidt, "Coherent measurements with MIMO radar networks of incoherent FMCW sensor nodes," *IEEE Microw. Wireless Compon. Lett.*, vol. 30, no. 7, pp. 721–724, Jul. 2020.
[37] D. Werbunat et al., "On the synchronization of uncoupled multistatic PMCW radars," *IEEE Trans. Microw. Theory Techn.*, vol. 72, no. 8, pp. 4932–4944, Aug. 2024.
[38] J. Aguilar, D. Werbunat, V. Janoudi, C. Bonfert, and C. Waldschmidt, "Uncoupled digital radars creating a coherent sensor network," *IEEE J. Microw.*, vol. 4, no. 3, pp. 459–472, Jul. 2024.
[39] L. Podbregar, A. Blatnik, S. Tomažic, and B. Batagelj, "Feasibility study of time synchronization solution for the bistatic synthetic aperture radar using mobile platforms," in *Proc. Int. Conf. Broadband Commun. Next Gener. Netw. Multimedia Appl. (CoBCom)*, Jul. 2024, pp. 1–6.
[40] B. Meinecke, M. Steiner, J. Schlichenmaier, J. Hasch, and C. Waldschmidt, "Coherent multistatic MIMO radar networks based on repeater tags," *IEEE Trans. Microw. Theory Techn.*, vol. 67, no. 9, pp. 3908–3916, Sep. 2019.
[41] A. Grathwohl, B. Meinecke, M. Widmann, J. Kanz, and C. Waldschmidt, "UAV-based bistatic SAR-imaging using a stationary repeater," *IEEE J. Microw.*, vol. 3, no. 2, pp. 625–634, Apr. 2023.
[42] G. Krieger et al., "MirrorSAR: A fractionated space radar for bistatic, multistatic and high-resolution wide-swath SAR imaging," in *Proc. IEEE Int. Geosci. Remote Sens. Symp. (IGARSS)*, Jul. 2017, pp. 149–152.
[43] K. Kulpa, M. Malanowski, P. Samczynski, and B. Dawidowicz, "The concept of airborne passive radar," in *Proc. Microw., Radar Remote Sens. Symp.*, Aug. 2011, pp. 267–270.
[44] M. Antoniou, Z. Zeng, L. Feifeng, and M. Cherniakov, "Experimental demonstration of passive BSAR imaging using navigation satellites and a fixed receiver," *IEEE Geosci. Remote Sens. Lett.*, vol. 9, no. 3, pp. 477–481, May 2012.
[45] D. Gromek, K. Kulpa, and P. Samczynski, "Experimental results of passive SAR imaging using DVB-T illuminators of opportunity," *IEEE Geosci. Remote Sens. Lett.*, vol. 13, no. 8, pp. 1124–1128, Aug. 2016.
[46] L. M. H. Ulander, P.-O. Frölind, A. Gustavsson, R. Ragnarsson, and G. Stenström, "Airborne passive SAR imaging based on DVB-T signals," in *Proc. IEEE Int. Geosci. Remote Sens. Symp. (IGARSS)*, Jul. 2017, pp. 2408–2411.
[47] B. Gabard, V. Wasik, O. Rabaste, T. Deloues, D. Poullin, and H. Jeuland, "Airborne targets detection by UAV-embedded passive radar," in *Proc. 17th Eur. Radar Conf. (EuRAD)*, Jan. 2021, pp. 346–349.
[48] N. Souli, P. Kardaras, P. Kolios, and G. Ellinas, "Onboard passive radar system implementation for detection and tracking of rogue UAVs," in *Proc. Int. Conf. Unmanned Aircr. Syst. (ICUAS)*, Jun. 2023, pp. 820–826.
[49] F. Colone, F. Filippini, and D. Pastina, "Passive radar: Past, present, and future challenges," *IEEE Aerosp. Electron. Syst. Mag.*, vol. 38, no. 1, pp. 54–69, Jan. 2023.
[50] M. Horlbeck, B. Scheiner, R. Weigel, and F. Lurz, "Overview of passive radar and its receiver architectures to enhance safety in civil aviation: A comprehensive analysis of history, principles, and performance optimization strategies," *IEEE Microw. Mag.*, vol. 25, no. 5, pp. 53–71, May 2024.
[51] M. Younis, R. Metzig, and G. Krieger, "Performance prediction of a phase synchronization link for bistatic SAR," *IEEE Geosci. Remote Sens. Lett.*, vol. 3, no. 3, pp. 429–433, Jul. 2006.
[52] M. García-Fernández, G. Álvarez-Narciandi, Y. Álvarez López, and F. Las-Heras Andrés, "Analysis and validation of a hybrid forward-looking down-looking ground penetrating radar architecture," *Remote Sens.*, vol. 13, no. 6, p. 1206, Mar. 2021.
[53] M. Ash, M. Ritchie, K. Chetty, and P. V. Brennan, "A new multistatic FMCW radar architecture by over-the-air deramping," *IEEE Sensors J.*, vol. 15, no. 12, pp. 7045–7053, Dec. 2015.
[54] K. Lee, S. Bahrami, K.-H. Kim, J. Kim, S.-U. Choi, and H.-J. Song, "Mono/multistatic mode-configurable E-band FMCW radar transceiver module for drone-borne synthetic aperture radar," in *Proc. IEEE Radio Freq. Integr. Circuits Symp. (RFIC)*, Jun. 2023, pp. 237–240.
[55] J. M. Merlo, S. R. Mghabghab, and J. A. Nanzer, "Wireless picosecond time synchronization for distributed antenna arrays," *IEEE Trans. Microw. Theory Techn.*, vol. 71, no. 4, pp. 1720–1731, Apr. 2023.
[56] A. Grathwohl, B. Arendt, T. Grebner, and C. Waldschmidt, "Detection of objects below uneven surfaces with a UAV-based GPSAR," *IEEE Trans. Geosci. Remote Sens.*, vol. 61, 2023, Art. no. 5207913.
[57] P. Schoeder, B. Schweizer, A. Grathwohl, and C. Waldschmidt, "Multitarget simulator for automotive radar sensors with unknown chirp-sequence modulation," *IEEE Microw. Wireless Compon. Lett.*, vol. 31, no. 9, pp. 1086–1089, Sep. 2021.
[58] D. M. Pozar, *Microwave Engineering*, 4th ed., Chichester, U.K.: Wiley, Nov. 2011.
[59] E. C. Zaugg and D. G. Long, "Generalized frequency scaling and backprojection for LFM-CW SAR processing," *IEEE Trans. Geosci. Remote Sens.*, vol. 53, no. 7, pp. 3600–3614, Jul. 2015.
[60] M. I. Skolnik, *Radar Handbook*, 3rd ed., Boston, MA, USA: McGraw-Hill, 2008.
[61] J. Kanz, A. Grathwohl, and C. Waldschmidt, "Surface clutter analysis for detectability prediction of buried objects with a UAV-based GPSAR," in *Proc. Eur. Radar Conf. (EuRAD)*, Sep. 2023, pp. 221–224.
[62] R. Burr, M. Schartel, W. Mayer, T. Walter, and C. Waldschmidt, "Lightweight broadband antennas for UAV based GPR sensors," in *Proc. 15th Eur. Radar Conf. (EuRAD)*, Sep. 2018, pp. 245–248.
[63] R. Bähnemann et al., "Under the sand: Navigation and localization of a micro aerial vehicle for landmine detection with ground-penetrating synthetic aperture radar," *Field Robot.*, vol. 2, pp. 1028–1067, Jun. 2022.
[64] M. Hisatsu, S. Mori, M. Arakawa, and H. Kanai, "Generalized coherence factor estimated from real signals in ultrasound beamforming," *J. Med. Ultrason.*, vol. 47, no. 2, pp. 179–192, Jan. 2020.
[65] H. Rudolf, D. Tarchi, and A. J. Sieber, "Combination of linear and circular SAR for 3-D features," in *Proc. IEEE Int. Geosci. Remote Sens. Symp.*, vol. 4, Jun. 1997, pp. 1551–1553.
[66] J. A. Jackson, B. D. Rigling, and R. L. Moses, "Canonical scattering feature models for 3D and bistatic SAR," *IEEE Trans. Aerosp. Electron. Syst.*, vol. 46, no. 2, pp. 525–541, Apr. 2010.

Julian Kanz (Graduate Student Member, IEEE) received the B.Sc. and M.Sc. degrees in electrical engineering from Ulm University, Ulm, Germany, in 2019 and 2022, respectively, where he is currently pursuing the Ph.D. degree with the Institute of Microwave Engineering.

His research interests include system concepts for multistatic radar networks on uncrewed aerial vehicles (UAVs) and high-resolution synthetic aperture radar processing.

Christina Bonfert (nee Knill) (Member, IEEE) received the Dr.-Ing. degree in electrical engineering from Ulm University, Ulm, Germany, in 2021.

From 2015 to 2021, she was a Research Assistant with the Institute of Microwave Engineering, Ulm University, where her doctoral research focused on orthogonal frequency-division multiplexing (OFDM) radar, novel digital radar signal processing methods, and signal design for digital radars. Since 2022, she has been a Post-Doctoral Researcher with the Institute of Microwave Engineering, Ulm University. Her current research interests include signal processing and compressed sensing for uncrewed aerial vehicle (UAV)-based synthetic aperture radar (SAR) systems and applications.

Dr. Bonfert was the Co-Chair of European Radar Conference (EuRAD) in 2023.

Christian Gesell (Graduate Student Member, IEEE) received the B.Sc. and M.Sc. degrees in electrical engineering from Ulm University, Ulm, Germany, in 2021 and 2024, respectively, where he is currently pursuing the Ph.D. degree with the Institute of Microwave Engineering, with a focus on digital radar systems and synthetic aperture radar processing.

Alexander Grathwohl (Graduate Student Member, IEEE) received the master's degree in electrical engineering from Ulm University, Ulm, Germany, in 2019, where he is currently pursuing the Ph.D. degree in electrical engineering with the Institute of Microwave Engineering.

From 2017 to 2018, he was an Intern with EAA, Bosch Sensortec, Sunnyvale, CA, USA. His research interests include uncrewed aerial vehicle (UAV)-based synthetic aperture radar (SAR) systems for high-resolution surface and subsurface imaging and their applications.

Frederik Bormuth (Graduate Student Member, IEEE) received the M.Sc. degree in electrical engineering from Ulm University, Ulm, Germany, in 2023, where he is currently pursuing the Ph.D. degree with the Institute of Microwave Engineering.

His research interests include wave propagation through layered media for improved uncrewed aerial vehicle (UAV)-based synthetic aperture radar (SAR) imaging.

Gerhard Krieger (Fellow, IEEE) received the Dipl.-Ing. (M.S.) and Dr.-Ing. (Ph.D.) (Hons.) degrees in electrical and communication engineering from the Technical University of Munich, Munich, Germany, in 1992 and 1999, respectively.

From 1992 to 1999, he was with Ludwig Maximilians University, Munich, where he conducted multidisciplinary research on neuronal modeling and nonlinear information processing in biological and technical vision systems. Since 1999, he has been with the Microwaves and Radar Institute, German Aerospace Center (DLR), Oberpfaffenhofen, Weßling, Germany, where he started as a Research Associate developing signal processing algorithms for a novel forward-looking radar system using digital beamforming on receive. From 2001 to 2007, he led the New SAR Missions Group which pioneered the development of advanced bistatic and multistatic radar systems, such as TanDEM-X, as well as innovative multichannel SAR techniques and algorithms for high-resolution wide-swath SAR imaging. Since 2008, he has been the Head of the Radar Concepts Department which currently hosts about 60 scientists focusing on new SAR techniques, missions, and applications. He has been serving as a Mission Engineer for TanDEM-X and he also made major contributions to the development of the Tandem-L mission concept, where he led the Phase-0 and Phase-A studies. Since 2019, he holds also a professorship at the Friedrich-Alexander-University Erlangen, Erlangen, Germany, and he is the author or a co-author of more than 100 peer-reviewed journal articles, nine invited book chapters, about 500 conference papers, and more than 30 patents.

Prof. Krieger received several national and international awards, including two Best Paper Awards at European Conference on Synthetic Aperture Radar, two Transactions Prize Paper Awards of the IEEE Geoscience and Remote Sensing Society, and the W. R. G. Baker Prize Paper Award from the IEEE Board of Directors. In 2014 and 2024, he served as the Technical Program Chair for European Conference on Synthetic Aperture Radar and in 2014 also as a Guest Editor for IEEE JOURNAL OF SELECTED TOPICS IN APPLIED EARTH OBSERVATIONS AND REMOTE SENSING. He has been an Associate Editor of IEEE TRANSACTIONS ON GEOSCIENCE AND REMOTE SENSING since 2012.

Christian Waldschmidt (Fellow, IEEE) received the Dipl.-Ing. (M.S.E.E.) and Dr.-Ing. (Ph.D.E.E.) degrees from University Karlsruhe (TH), Karlsruhe, Germany, in 2001 and 2004, respectively.

From 2001 to 2004, he was a Research Assistant at the Institut fur Hochstfrequenztechnik and Elektronik (IHE), Karlsruhe; and Universitat Karlsruhe (TH). Since 2004, he has been with Robert Bosch GmbH, Renningen, Germany, with the Business Units Corporate Research and Chassis Systems. He was heading different research and development teams in microwave engineering, RF-sensing, and automotive radar. In 2013, he returned to academia. He was appointed as the Director of the Institute of Microwave Engineering, Ulm University, Ulm, Germany, as a Full Professor. He authored or co-authored more than 320 scientific publications and more than 25 patents. His research interests include radar and RF sensing, mm-wave and submillimeter-wave engineering, antennas and antenna arrays, and RF and array signal processing.

Dr. Waldschmidt has been a member of the Heidelberg Academy of Sciences and Humanities since 2020 and a member of the National Academy of Science and Engineering since 2024. He was a co-recipient of more than 15 best paper awards since 2015. He served as the Chair for the IEEE MTT-29 Technical Committee on Microwave Aerospace Systems and the MTT-27 Technical Committee on Wireless Enabled Automotive and Vehicular Applications. He was a two-time TPC Chair and the General Chair of the IEEE MTT International Conference on Microwaves for Intelligent Mobility. In 2022, he was the General Chair of German Microwave Conference and in 2023 General Chair of European Radar Conference (EuRAD). He was a three-time Guest Editor of *IEEE Microwave Magazine* and IEEE MICROWAVE AND WIRELESS COMPONENTS LETTERS (MWCL). From 2018 to 2022, he served as an Associate Editor for IEEE MWCL. He is a reviewer for multiple IEEE TRANSACTIONS and many IEEE conferences in the field of microwaves.